

## Exploring maverick top partner decays at the LHC

Shivam Verma<sup>1,\*</sup> Sanjoy Biswas<sup>1,†</sup> Anirban Chatterjee<sup>2,‡</sup> and Joy Ganguly<sup>3,§</sup>

<sup>1</sup>*Department of Physics, Ramakrishna Mission Vivekananda Educational and Research Institute, Belur Math, Howrah 711202, India*

<sup>2</sup>*Department of Physics, Indian Institute of Technology, Kanpur 208016, India*

<sup>3</sup>*Department of Physics, Indian Institute of Technology, Hyderabad 502285, India*



(Received 15 October 2022; accepted 23 May 2023; published 16 June 2023)

In this work, we have considered an extension of the standard model (SM) with a  $SU(2)_L$  singlet vectorlike quark (VLQ) with electric charge  $Q = +2/3$ . The model also contains an additional local  $U(1)_d$  symmetry group and the corresponding gauge boson is the dark photon. The VLQ is charged while all the SM particles are neutral under the new  $U(1)_d$  gauge group. Even though in this model the VLQ possesses many properties qualitatively similar to that of the traditional top partner ( $T_p$ ), there are some compelling differences as well. In particular, its branching ratio to the traditional modes ( $T_p \rightarrow bW, tZ, th$ ) are suppressed which in turn helps to evade many of the existing bounds, mainly coming from the LHC experiments. In an earlier work, such a VLQ is referred to as “maverick top partner”. It has been shown that the top partner in this model predominantly decays to a top quark and a dark photon/dark Higgs pair ( $T_p \rightarrow t\gamma_d, th_d$ ) over a large region of the parameter space. The dark photon can be made invisible and consequently, it gives rise to the missing transverse energy ( $\cancel{E}_T$ ) signature at the LHC detector. We have mainly focused on the LHC signatures and future prospects of such top partners. In particular, we have studied the  $t\bar{t} + \cancel{E}_T$  and  $t + \cancel{E}_T$  signatures in the context of the LHC via pair and single productions of the top partner, respectively at 13 and 14 TeV LHC center of mass energies assuming that the dark photon either decays into an invisible mode or it is invisible at the length scale of the detector. We have shown that one can exclude  $\sin\theta_L \sim 0.025$  (0.05) for  $m_{T_p} \leq 2.0$  (2.6) TeV at  $\sqrt{s} = 14$  TeV with an integrated luminosity of  $3 \text{ ab}^{-1}$  using the single top partner production channel.

DOI: [10.1103/PhysRevD.107.115024](https://doi.org/10.1103/PhysRevD.107.115024)

### I. INTRODUCTION

Search for new resonances or particle-like states predicted by the physics beyond the Standard Model (BSM) is an important goal for the Large Hadron Collider (LHC). One of the foremost among them is search for vectorlike fermions (VLFs), in particular, vectorlike quarks (VLQs). VLQs are omnipresent in many extensions of the SM such as SM with extra dimension [1–3], composite Higgs model [4–6], primarily motivated to solve the Higgs mass problem in the SM [7–9]. A lot of studies has been done on the phenomenological aspects of VLQs in a general setup [10–27]. However, the existence of VLQ (or VLF in

general) can also be motivated in a class of theories where the SM is augmented with a dark sector (DS) and the VLFs act as mediators between the visible and the DS (often referred as portal matter) [28–31]. The DS in its most simple form can contain a dark photon [32] corresponding to a dark  $U(1)_d$  gauge symmetry. In many extensions of the SM motivated by the solution to the dark matter (DM) problem, dark photon is introduced in order to explain the small scale structure of the universe [33].

The theoretical framework considered in this study closely follows that of Ref. [34]. We have considered a  $SU(2)_L$  singlet vectorlike quark carrying  $+2/3$  unit of electric charge. The VLQ is also charged under an additional  $U(1)_d$  dark gauge symmetry whereas all the SM fields are neutral under this new symmetry. The  $U(1)_d$  symmetry is spontaneously broken by the vacuum expectation value (VEV) of a complex scalar field (dark Higgs) and the gauge boson (dark photon) corresponding to the local  $U(1)_d$  symmetry becomes massive. The dark Higgs field is not only responsible for giving mass to the dark photon in this framework but it also plays an important role, namely, it induces a mixing between the top-quark and the VLQ. We will only consider the VLQ mixing with the 3rd

\*shivam.59910103@gm.rkmvu.ac.in

†sanjoy.phy@gm.rkmvu.ac.in

‡anirbanc@iitk.ac.in

§joyganguly.hep2022@gmail.com

Published by the American Physical Society under the terms of the [Creative Commons Attribution 4.0 International license](https://creativecommons.org/licenses/by/4.0/). Further distribution of this work must maintain attribution to the author(s) and the published article's title, journal citation, and DOI. Funded by SCOAP<sup>3</sup>.

TABLE I. Representations of the relevant field content under the full symmetry group of the theory. The remaining SM fields are all neutral under the new  $U(1)_d$ .

Fields	$SU(3)_C$	$SU(2)_L$	$Y$	$Y_d$
$t'_R$	3	1	2/3	0
$b_R$	3	1	-1/3	0
$Q_L = \begin{pmatrix} t'_L \\ b_L \end{pmatrix}$	3	2	1/6	0
$\Phi$	1	2	1/2	0
$T'_L$	3	1	2/3	1
$T'_R$	3	1	2/3	1
$\Phi_d$	1	1	0	1

generation quark with same charge. However, as we will see later on, the vectorlike quark being charged under the additional  $U(1)_d$  gauge interaction, its branching ratio into the traditional decay modes ( $T_p \rightarrow bW, tZ, th$ ) are all suppressed. In this framework, it predominantly decays to a top-quark and a dark photon/dark Higgs ( $T_p \rightarrow t\gamma_d, th_d$ ). Such a VLQ having same electric charge and color quantum number as that of SM top-quark with traditional decay modes suppressed is referred to as ‘‘maverick top partner’’ in [34]. Similar extensions with VLQs carrying  $-1/3$  unit of electric charge was earlier proposed in [28,29] which also predicts an enhanced branching ratio of the bottom partner to the non-standard modes. The origin of this enhancement in branching ratio to the non-standard modes can be traced back to the hierarchies between (i) the top and the maverick top partner masses, (ii) the vacuum expectation values of the two Higgs fields and (iii) the fermion mass ratio and the fermion mixing angle. The existence of such a top partner, not only gives rise to rich collider phenomenology but also helps to evade the constraints coming from the LHC data depending on their transformation properties under the SM gauge group. The collider constraints come from pair production of top partner or single production of top partner in association with a forward jet at the LHC. The current LHC data is mostly sensitive to VLQ searches in the traditional decay modes ( $T_p \rightarrow bW, tZ, th$ ) [35–38]. Nonstandard or exotic decays of the vectorlike quarks in different setups with different collider signatures have been considered in the literature [39–49].

In the present work, we will assume that the dark photon always decays to a pair of DM particles. Consequently, in a collider experiment the signature of the dark photon production will be *missing momentum*. Our motivation is to constrain the decay of the maverick top partner into a top-quark and dark photon pair at the LHC in the  $t\bar{t} + \cancel{E}_T$  and  $t + \cancel{E}_T$  channels and for that it is sufficient to treat the dark photon and its subsequent decay products to be invisible at the length scale of the detector. The details of the DM sector and its phenomenology is not considered here. We emphasize that

the allowed region of the parameter space that is consistent with the perturbative unitarity and electroweak precision (EWP) measurements [50–52] can be excluded at the high-luminosity (HL) LHC. We have also set the exclusion limit on the relevant parameter space using the latest LHC data in the  $t\bar{t} + \cancel{E}_T$  and  $t + \cancel{E}_T$  channels [53–55].

The rest of the paper is organized as follows: In Sec. II, we briefly outline the theoretical framework considered for the present analysis including various constraints on the model parameters. The event selection for both the single and pair production of maverick top partner(s) is detailed in Sec. III. In Sec. IV, we present the results of our numerical simulation and discuss their significances. Finally, we conclude in Sec. V.

## II. THEORETICAL FRAMEWORK

In this section, we briefly summarize the theoretical framework proposed in [34]. The model contains a  $SU(2)_L$  singlet vectorlike quark having electric charge  $+2/3$  unit. The top partner is also charged under an additional  $U(1)_d$  dark gauge symmetry. The gauge boson corresponding to the local  $U(1)_d$  symmetry is the dark photon (in the limit of very tiny kinetic mixing). The model also contains a complex scalar field  $\Phi_d$  charged under the  $U(1)_d$  and singlet under the SM gauge group. The dark photon becomes massive as  $\Phi_d$  develops a nonzero vacuum expectation value,  $\langle \Phi_d \rangle = v_d/\sqrt{2}$ . The corresponding Higgs mode in the dark sector after mixing with the SM Higgs gives a dark Higgs in the mass eigenbasis. All the SM fields are neutral under the  $U(1)_d$ . The full Lagrangian of the model is detailed below:

The relevant fields content and their representations under  $SU(3)_C \times SU(2)_L \times U(1)_Y \times U(1)_d$  symmetry groups are summarized in Table I.

The relevant sectors of the Lagrangian invariant under  $SU(3)_C \times SU(2)_L \times U(1)_Y \times U(1)_d$  symmetry group are given below:

$$\mathcal{L}_{\text{Gauge}} = -\frac{1}{4} G_{\mu\nu}^a G^{a,\mu\nu} - \frac{1}{4} W_{\mu\nu}^i W^{i,\mu\nu} - \frac{1}{4} B'_{\mu\nu} B'^{\mu\nu} + \frac{\epsilon'}{2 \cos \theta_W} B'_{d,\mu\nu} B'^{\mu\nu} - \frac{1}{4} B'_{d,\mu\nu} B'^{\mu\nu}, \quad (1)$$

where  $G_{\mu\nu}^a$  are the  $SU(3)_C$  field strength tensor with  $a = 1, \dots, 8$ ,  $W_{\mu\nu}^i$  are  $SU(2)_L$  field strength tensor with  $i = 1, 2, 3$ ,  $B'_{\mu\nu}$  is that of the  $U(1)_Y$  and  $B'_{d,\mu\nu}$  corresponds the field strength tensor of the additional  $U(1)_d$ . The kinetic mixing term is parametrized by  $\epsilon'$ .

$$\mathcal{L}_{\text{Scalar}} = |D_\mu \Phi|^2 + |D_\mu \Phi_d|^2 - V(\Phi, \Phi_d) \quad (2)$$

where  $\Phi$  and  $\Phi_d$  are the SM and dark sector Higgs fields, respectively and the corresponding scalar potential is given by

$$V(\Phi, \Phi_d) = -\mu^2 |\Phi|^2 + \lambda |\Phi|^4 - \mu_{h_d}^2 |\Phi_d|^2 + \lambda_{h_d} |\Phi_d|^4 + \lambda_{hh_d} |\Phi|^2 |\Phi_d|^2. \quad (3)$$

The gauge covariant derivative has the form

$$D_\mu = \partial_\mu - ig_s t^a G_\mu^a - ig T^i W_\mu^i - ig' Y B_\mu - ig'_d Y_d B'_{d,\mu}. \quad (4)$$

Here,  $g_s, g, g', g'_d$  are the  $SU(3)_C, SU(2)_L, U(1)_Y$  and  $U(1)_d$  couplings constants, respectively and  $t^a$ 's and  $T^i$ 's are the generators of the  $SU(3)_C$  and  $SU(2)_L$  groups, respectively.

When the  $SU(3)_C \times SU(2)_L \times U(1)_Y \times U(1)_d$  symmetry is spontaneously broken to  $SU(3)_C \times U(1)_{\text{em}}$  by the choice of minimum value configurations of  $\Phi$  and  $\Phi_d$  which in unitary gauge can be written as

$$\Phi = \begin{pmatrix} 0 \\ \frac{v_{\text{EW}} + h'}{\sqrt{2}} \end{pmatrix}, \quad \Phi_d = \frac{1}{\sqrt{2}}(v_d + h'_d). \quad (5)$$

one ends up with two massive scalar modes (and massive gauge bosons of the corresponding broken gauge groups). Here,  $v_{\text{EW}}$  has value 246 GeV.

To find the mass basis we rotate  $h'$  and  $h'_d$  as

$$\begin{pmatrix} h \\ h_d \end{pmatrix} = \begin{pmatrix} \cos \theta_S & -\sin \theta_S \\ \sin \theta_S & \cos \theta_S \end{pmatrix} \begin{pmatrix} h' \\ h'_d \end{pmatrix} \quad (6)$$

The  $h$  can be identified as the observed Higgs boson with mass  $m_h = 125$  GeV while  $h_d$  can be taken as BSM Higgs with mass  $m_{h_d}$ . Hence, the free parameters are  $\theta_S, m_{h_d}$  and  $v_d$  as all the other parameters in the potential of Eq. (3) can be expressed in terms of the above-mentioned free parameters.

The full Lagrangian for the fermion sector involving 3rd generation quarks and VLQ is given by

$$\mathcal{L}_{\text{Fermion}} = \bar{Q}_L i \not{D} Q_L + \bar{T}'_R i \not{D} T'_R + \bar{b}_R i \not{D} b_R + \bar{T}' i \not{D} T' + \mathcal{L}_{\text{Yuk}} \quad (7)$$

where,  $\mathcal{L}_{\text{Yuk}}$  is given by

$$\mathcal{L}_{\text{Yuk}} = -y_b \bar{Q}_L \Phi b_R - y_t \bar{Q}_L \tilde{\Phi} t'_R - \lambda_T \Phi_d \bar{T}'_L t'_R - m_T \bar{T}'_L T'_R + \text{H.c.} \quad (8)$$

when  $\Phi$  and  $\Phi_d$  get VEVs, mass matrix in  $t'$  and  $T'$  basis can be written in a form as

$$\mathcal{L}_{u3\text{-mass}} = -\bar{\chi}_L \mathcal{M} \chi_R + \text{H.c.}, \quad (9)$$

where,

$$\chi_\tau = \begin{pmatrix} t'_\tau \\ T'_\tau \end{pmatrix}, \quad \mathcal{M} = \begin{pmatrix} \frac{y_t v_{\text{EW}}}{\sqrt{2}} & 0 \\ \frac{\lambda_T v_d}{\sqrt{2}} & m_T \end{pmatrix}, \quad (10)$$

Here  $\tau = L, R$ .

One requires the biunitary transformation of the following kind in order to diagonalize the above mass matrix

$$\begin{pmatrix} t_L \\ T_{pL} \end{pmatrix} = \begin{pmatrix} \cos \theta_L & -\sin \theta_L \\ \sin \theta_L & \cos \theta_L \end{pmatrix} \begin{pmatrix} t'_L \\ T'_L \end{pmatrix}, \quad \begin{pmatrix} t_R \\ T_{pR} \end{pmatrix} = \begin{pmatrix} \cos \theta_R & -\sin \theta_R \\ \sin \theta_R & \cos \theta_R \end{pmatrix} \begin{pmatrix} t'_R \\ T'_R \end{pmatrix} \quad (11)$$

Here  $t$  can be identified as the SM top quark having mass  $m_t = 173.2$  GeV. The fermion sector contains two free parameters: the mass of top partner,  $m_{T_p}$  and the mixing angle involving the left-handed fields,  $\theta_L$ . We take  $\sin \theta_L, m_t$  and  $m_{T_p}$  as independent parameters for the rest of the discussion.

To verify the allowed ranges of  $\sin \theta_L$  consistent with perturbative unitarity we trade Eq. (B26) to write  $\sin \theta_L$  as

$$|\sin \theta_L| = \frac{1}{2} \sqrt{\frac{2m_{T_p}^2 - 2m_t^2 - \lambda_T^2 v_d^2}{m_{T_p}^2 - m_t^2} \left( 1 - \sqrt{1 - \frac{8\lambda_T^2 v_d^2 m_t^2}{(2m_{T_p}^2 - 2m_t^2 - \lambda_T^2 v_d^2)^2}} \right)} \quad (12)$$

To have real solution for  $\sin \theta_L$  one needs  $|\lambda_T| < \sqrt{2}(m_{T_p} - m_t)/v_d$ . On the other hand the perturbative unitarity bound on  $\lambda_T$  requires  $\lambda_T < 4\sqrt{2}\pi$ .<sup>1</sup> We can combine these two conditions and write

$$|\lambda_T| < \sqrt{2} \min \left( \frac{m_{T_p} - m_t}{v_d}, 4\sqrt{\pi} \right) \quad (13)$$

<sup>1</sup>The perturbative unitarity bound has been estimated by studying the  $h_d t \rightarrow h_d t$  scattering process in [34].

In Fig. 1, we illustrate the effect of Eq. (13) on the allowed ranges of  $\sin \theta_L$  as a function of the top partner mass.

Finally, the relevant parameters which play a crucial role in the discussion that follows are  $\sin \theta_L, v_d, m_{\gamma_d}, m_{h_d}$ , and  $m_{T_p}$ . These parameters can be considered as free, albeit with certain restrictions in their allowed ranges coming from various constraints such as perturbative unitarity bound, constraints coming from electroweak precision observables (EWPO) [51,52] and Higgs signal strength measurements.

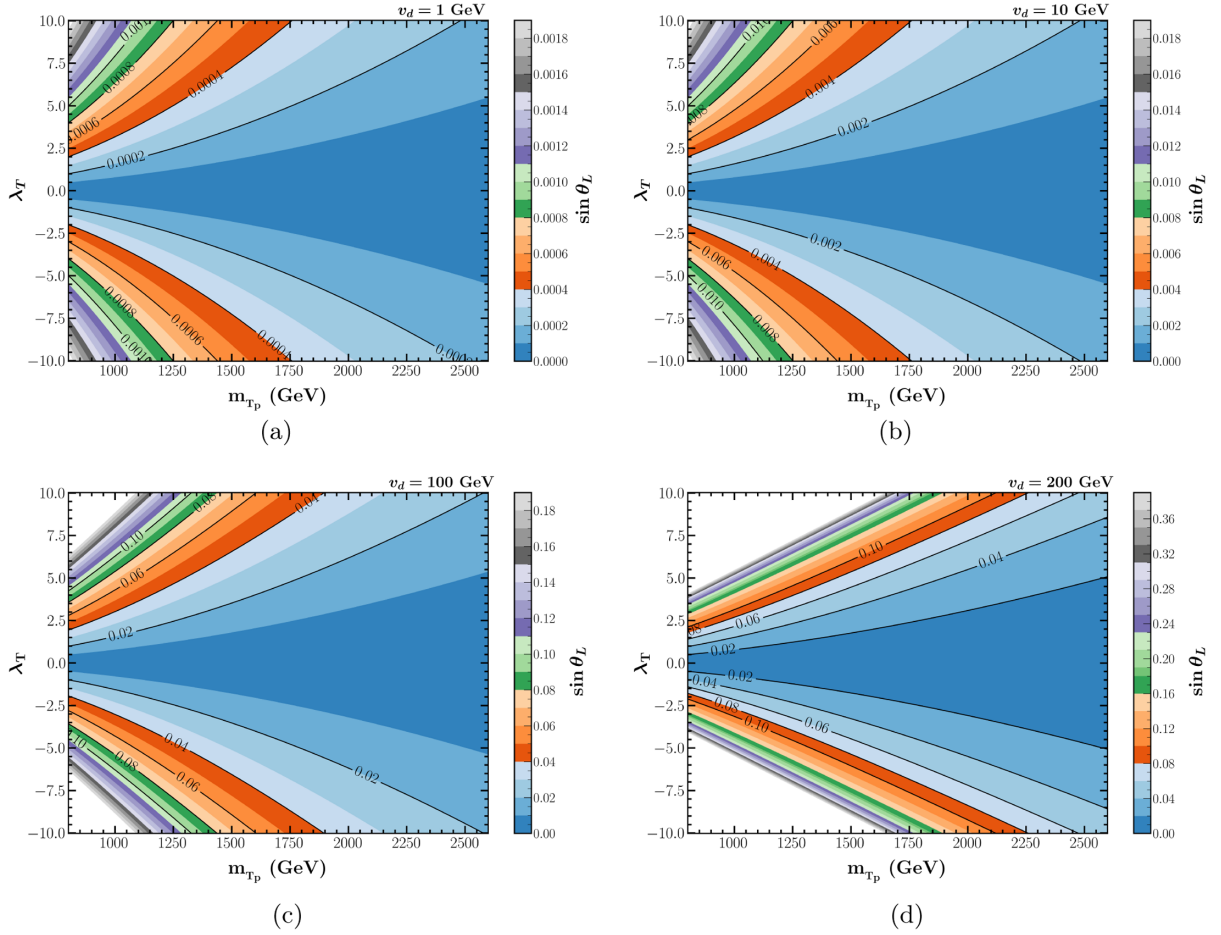


FIG. 1. Allowed ranges of  $\sin\theta_L$  in the  $\lambda_T - m_{T_p}$  plane for different choices of  $v_d$  consistent with perturbative unitarity bound.

The mixing angle between the SM Higgs and the dark Higgs is constrained by various observations [56–60]. For low mass region ( $10 \text{ GeV} \leq m_{h_d} \leq 100 \text{ GeV}$ ) there is a stringent lower limit (0.9–0.998) on the allowed values of  $|\sin\theta_S|$  for  $v_d \sim v_{EW}$  coming from LEP experiment.

For  $m_{h_d} > 100 \text{ GeV}$ , the constraint coming from LHC heavy Higgs searches and Higgs signal strength measurement are relevant and it depends on the mass of the dark Higgs. For  $m_{h_d} \sim 200\text{--}1000 \text{ GeV}$ , the Higgs signal strength measurement sets a limit on  $|\sin\theta_S| < 0.24$  [60]. However, heavy Higgs searches at the LHC give more stringent bound on  $|\sin\theta_S|$  in the range 200–600 GeV and the present upper limit on the allowed values of  $|\sin\theta_S|$  is 0.2 [59,60].

For higher masses, the constraint coming from the correction to W boson mass and the perturbative unitarity requirement is more stringent, for example,  $|\sin\theta_S|$  as low as 0.14 can be ruled out for  $m_{h_d} \sim 1 \text{ TeV}$  [60].

Exotic decays of the SM Higgs via the mixing of the SM Higgs with the dark Higgs also provides strong constraint on the scalar mixing angle which is sometimes more constraining than the bound coming from the Higgs signal

strengths measurements. For example, Higgs to invisible searches can be used to set limits on  $|\sin\theta_S|$  using the formula quoted in Ref. [34],

$$|\sin\theta_S| \leq 4.6 \times 10^{-4} \left( \frac{v_d}{\text{GeV}} \right) \sqrt{\text{BR}_{\text{lim}}} \quad (14)$$

where  $\text{BR}_{\text{lim}}$  is the upper limit on the branching ratio of the SM Higgs into invisible decay modes. The latest CMS [61] and ATLAS [62] searches for the Higgs  $\rightarrow$  invisible decay modes provide,

$$\text{BR}_{\text{lim}} = \begin{cases} 0.15 & \text{CMS} \\ 0.107 & \text{ATLAS} \end{cases} \quad (15)$$

For  $v_d = 100 \text{ GeV}$ , this translates to  $|\sin\theta_S| \leq 0.018$  (CMS) and 0.015 (ATLAS).

We define the ratio ( $R_\Gamma$ ) of the decay widths in the nonstandard and the standard (or traditional) modes as,

$$R_\Gamma = \frac{\Gamma(T_p \rightarrow t + h_d/\gamma_d)}{\Gamma(T_p \rightarrow t/b + W/Z/h)} \quad (16)$$

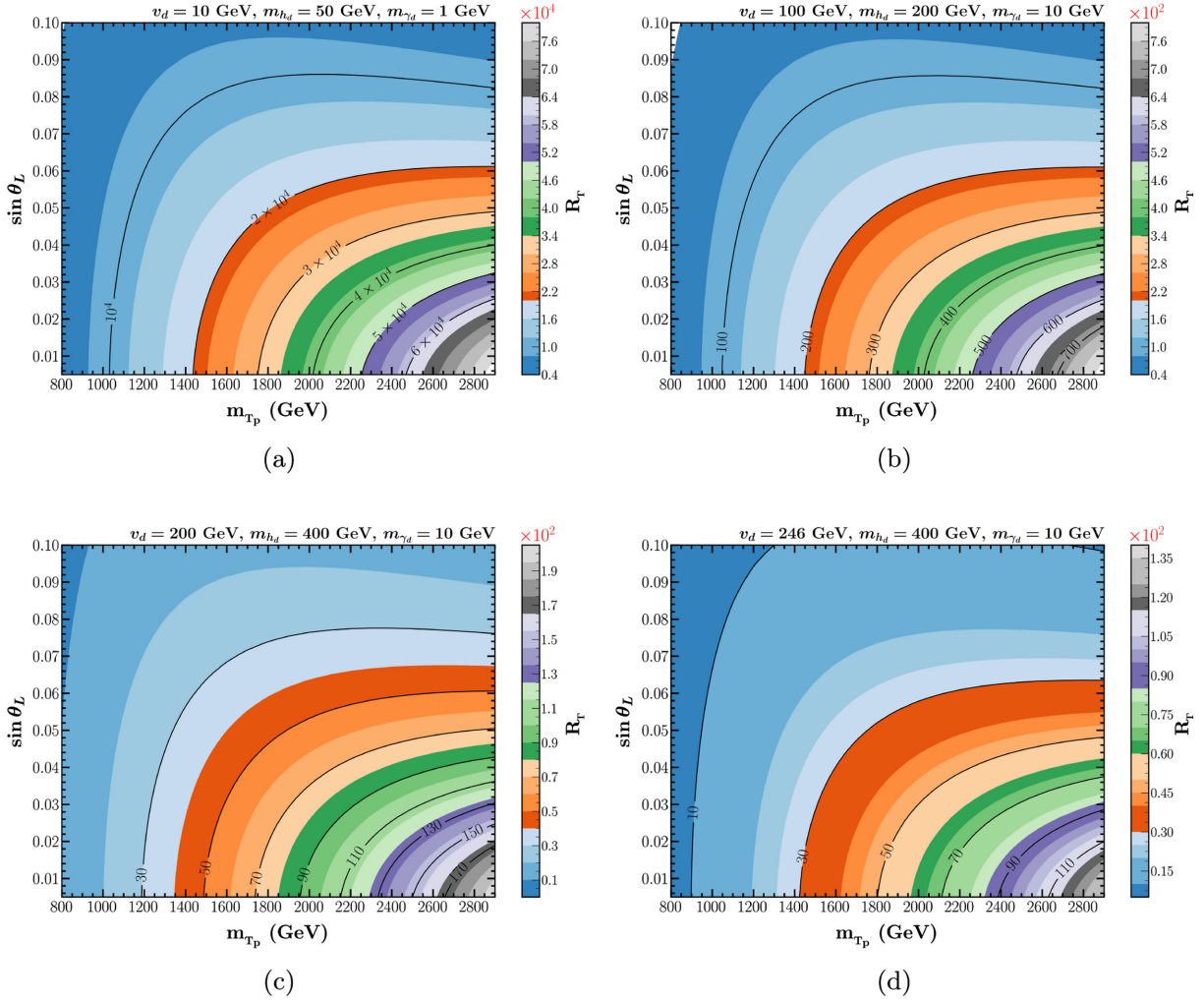


FIG. 2. Ratio of the decay widths in the non-standard ( $t\gamma_d, th_d$ ) and traditional ( $bW, tZ, th$ ) modes of the maverick top partner in the  $\sin \theta_L - m_{T_p}$  plane for different choices of  $v_d$  consistent with perturbative unitarity bound.

In the limit  $|\sin \theta_d|, |\sin \theta_S|, \varepsilon^2$  and  $m_t/m_{T_p} \ll 1$  this ratio is given by Eq. (17). It illustrates that the enhancement in the decay width in the nonstandard mode compared to that for the standard one in two different region of the parameter space in the  $\sin \theta_L - m_{T_p}$  plane significant for the HE-HL LHC analysis. In particular, at the HE-HL LHC both large  $m_{T_p}$  and small  $|\sin \theta_L|$  will be probed. Hence, it is important to consider the following two scenarios: (i)  $|\sin \theta_L| \ll m_t/m_{T_p} \ll 1$  and (ii)  $m_t/m_{T_p} \ll |\sin \theta_L| \ll 1$ , relevant for LHC.

$$R_\Gamma \approx \frac{1}{2} \begin{cases} \left(\frac{m_{T_p}}{m_t}\right)^2 \left(\frac{v_{EW}}{v_d}\right)^2 & \text{for } |\sin \theta_L| \ll \frac{m_t}{m_{T_p}} \ll 1 \\ \left(\frac{m_t}{m_{T_p} \sin^2 \theta_L}\right)^2 \left(\frac{v_{EW}}{v_d}\right)^2 & \text{for } \frac{m_t}{m_{T_p}} \ll |\sin \theta_L| \ll 1 \end{cases} \quad (17)$$

<sup>2</sup> $\varepsilon$  and  $\varepsilon'$  are related via  $\varepsilon = \varepsilon' / \sqrt{1 - \varepsilon'^2 / \cos^2 \hat{\theta}_W}$ , where  $\cos \hat{\theta}_W = \cos \theta_W + \mathcal{O}(\varepsilon^2)$ .

Eq. (17) explains when  $|\sin \theta_L| \ll m_t/m_{T_p} \ll 1$ , the enhancement in  $R_\Gamma$  has its origin in the hierarchy between the fermion masses ( $m_{T_p}/m_t$ ) and the two VEVs ( $v_{EW}/v_d$ ).

Whereas, in the other limit, i.e.,  $m_t/m_{T_p} \ll |\sin \theta_L| \ll 1$ <sup>3</sup> the enhancement can be traced back to the hierarchy between the two VEVs, i.e., ( $v_{EW}/v_d$ ) and that of  $m_t/(m_{T_p} \sin^2 \theta_L)$ . It shows even when  $v_d \sim v_{EW}$  one can have a small enhancement in  $R_\Gamma$  if,  $m_t/(m_{T_p} \sin^2 \theta_L) > 1$ , i.e., when  $\sin^2 \theta_L < m_t/m_{T_p} < |\sin \theta_L| \ll 1$ .

Figure 2 shows that the ratio of the decay widths ( $R_\Gamma$ ) of the top partner in the nonstandard and the traditional modes without making any approximation mentioned in Eq. (17). The  $R_\Gamma$  is calculated using Eq. (16) and supplying various decay widths provided in Appendix B.

<sup>3</sup>However, this region of parameter space is disfavored by perturbative unitarity constraint.

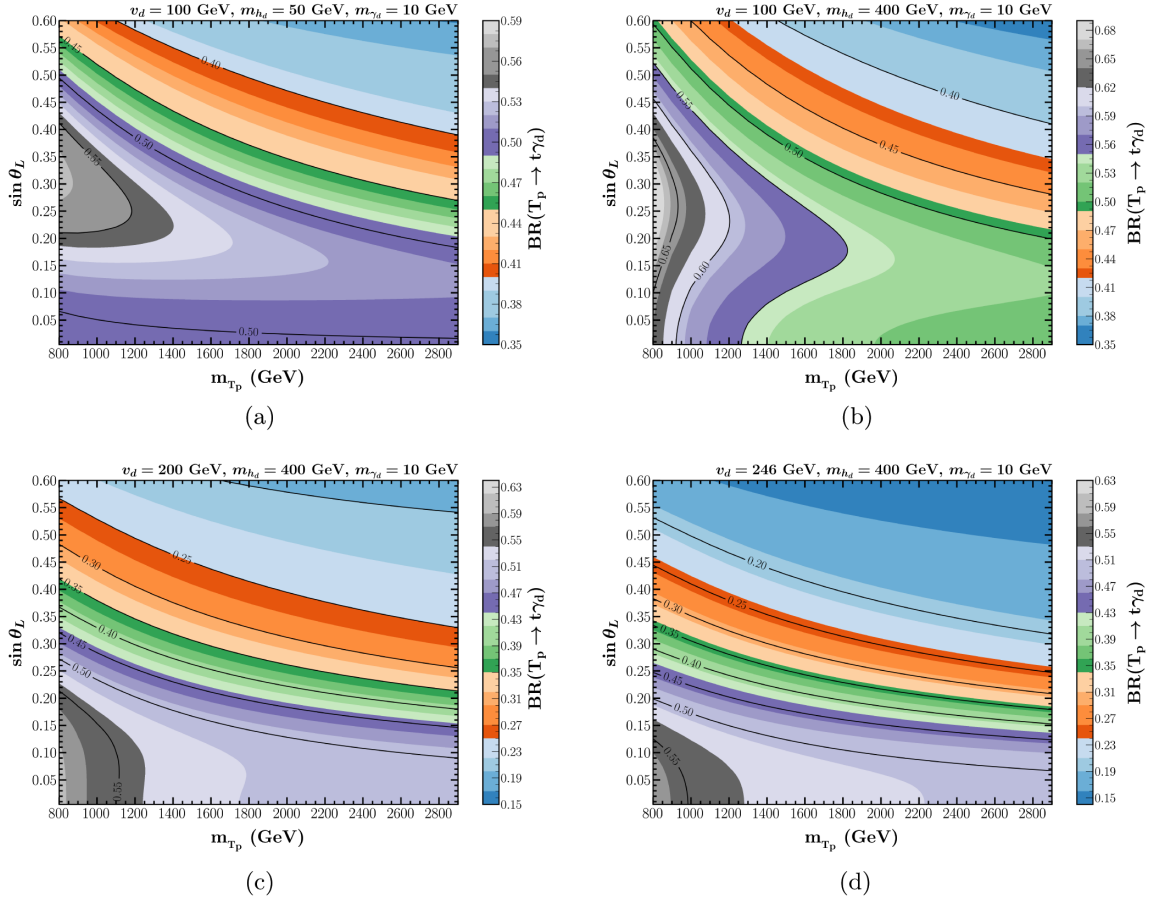


FIG. 3. Variation of the branching ratio of  $T_p \rightarrow t\gamma_d$  in the  $\sin\theta_L - m_{T_p}$  plane for several choices of  $v_d$ ,  $m_{\gamma_d}$ , and  $m_{h_d}$ .

To calculate various decay widths, we use the following values for the relevant SM parameters [63],

$$\begin{aligned}
 m_h &= 125.5 \text{ GeV}, & m_t &= 173.2 \text{ GeV}, & m_b &= 4.18 \text{ GeV} \\
 m_W &= 80.377 \text{ GeV}, & m_Z &= 91.187 \text{ GeV}, & v_{EW} &= 246 \text{ GeV}
 \end{aligned}$$

Throughout our analyses we set,  $|\sin\theta_S| = 10^{-6}$ .

The branching ratio in the  $\sin\theta_L - m_{T_p}$  plane is displayed in Fig. 3 for various choices of  $v_d$ ,  $m_{\gamma_d}$ , and  $m_{h_d}$ . In Table II we list the branching ratios of the top partner decaying into a top quark and a dark photon for various benchmark points. We have mostly restricted ourselves to the case of light dark photon in the mass range 1–10 GeV. In this mass range the corresponding bound on the kinetic mixing parameter ( $\epsilon$ ) is found to be  $\epsilon \lesssim 10^{-3}$  [64–66]. For

small kinetic mixing the  $U(1)_Y$  and  $U(1)_d$  gauge sectors remain practically decoupled and it hardly plays any role in the remaining discussions.

For the present analysis, we assume that the dark photon decays to an invisible mode (for example a pair of dark matter particles) so that it gives rise to  $\cancel{E}_T$  signature in a collider experiment. To achieve this, one needs to augment the present model with an additional dark sector particle charged under  $U(1)_d$  (a possible dark matter

TABLE II. Branching ratios of  $T_p \rightarrow t\gamma_d$  for various benchmark points, assuming  $\sin\theta_L = 0.1$ ,  $v_d = 200$  GeV,  $m_{\gamma_d} = 10$  GeV, and  $m_{h_d} = 400$  GeV.

$m_{T_p}$	800	1000	1200	1400	1600	1800	2000	2200	2400	2500	2600	2800
<b>BR</b>	0.593	0.560	0.542	0.531	0.522	0.516	0.511	0.507	0.503	0.502	0.500	0.497

candidate<sup>4,5</sup>). Throughout this article we, therefore, simply assume that the dark photon is invisible and evade any detection by the detector.

### III. TOP PARTNER AT THE LHC

In this section we describe in detail our collider analysis in the context of the LHC. We have considered both the single ( $pp \rightarrow T_p j$ ) and the pair ( $pp \rightarrow T_p \bar{T}_p$ ) production of top partner(s). We have used `MADGRAPH5_AMC@NLO` (version 3.2.0) [67] event generator to simulate both the single and pair production of top partner in the context of 13 and 14 TeV LHC energies. In order to achieve this, we have used `FeynRules` [68] where we have implemented the model described in Sec. II at the Lagrangian level. The Universal FeynRules Output [69] is then interfaced with `Madgraph5_AMC@NLO` for event generation. We have used parton distributions provided by NNPDF (version 2.3) [70] to simulate the parton-parton hard scattering in a  $pp$  collision. Events generated by `Madgraph` are then interfaced with `PYTHIA` (version 6.4)<sup>6</sup> [72] for parton shower, hadronization, and further analysis.

The energy and momenta of all the final state objects are smeared with appropriate Gaussian smearing function [73,74] to take into account the finite detector resolution effects and the resolution function considered is,

$$\frac{\sigma(x)}{x} = \frac{N}{x} \oplus \frac{S}{\sqrt{x}} \oplus C \quad (18)$$

where,  $x = p_T$  (for electron and muon) or  $E$  (for jet),  $N$  encapsulates the effect of electronic and pile-up noise,  $S$  characterizes stochastic effects arising from the sampling nature of calorimeters and  $C$  describes the  $x$  independent offset term.

We follow the functional form of resolution function as well as the fitted values of  $N$ ,  $S$ , and  $C$  parameters as given in Table III from default ATLAS card in DELPHES (version 3.5.0) [75].

Since the top partner dominantly decays to top-quark and a dark photon  $T_p \rightarrow t\gamma_d$  in our model, presence of top-quark is ubiquitous in both the single and pair production channels. We will mostly confine ourselves to the fully hadronic decay of the top-quark ( $t \rightarrow bW \rightarrow bqq'$ ). In the following we consider the top partner in the mass range  $1 \text{ TeV} (800 \text{ GeV}) \leq m_{T_p} \leq 2.6 (1.6) \text{ TeV}$  for the single

<sup>4</sup>We do not present explicit details of the DM content of the DS here. For more details we refer to [28].

<sup>5</sup>Alternatively, the dark photon can be made stable at the length scale of the detector provided the kinetic mixing parameter is very small ( $\lesssim 10^{-7}$ ).

<sup>6</sup>For  $pp \rightarrow \text{QCD multijet}$  simulation we have used `PYTHIA` (version 8.3) [71] in order to implement the jet parton matching.

TABLE III.  $N$ ,  $S$ , and  $C$  parameters for resolution function.

		$N$ (GeV)	$S$ (GeV) <sup>1/2</sup>	$C$
Jet	$\eta \leq 1.7$	1.59	0.521	0.030
	$1.7 < \eta \leq 3.2$	0	0.706	0.05
	$3.2 < \eta \leq 5.0$	0	1	0.0942
Electron	$\eta \leq 1.5$	0.05	0	$1.7 \times 10^{-3}$
	$1.5 < \eta \leq 2.5$	0.15	0	$3.1 \times 10^{-3}$
Muon	$\eta \leq 1.5$	0.015	0	$1.5 \times 10^{-4}$
	$1.5 < \eta \leq 2.5$	0.025	0	$3.5 \times 10^{-4}$

TABLE IV. Choices of  $R$ ,  $\delta p$ ,  $\delta r$  for various total transverse momentum range.

$E_{\text{tot}}$	400	600	800	1000	1600	2600
$R$	1.4	1.2	1.0	0.8	0.6	0.4
$\delta p$	0.10	0.10	0.05	0.05	0.05	0.05
$\delta r$	0.19	0.19	0.19	0.19	0.19	0.19

(pair) production of the top partner at the LHC. The top-quarks thus produced in the decay of the top partners are highly boosted for most of the ranges of top partner mass. Hence, the top decay products are highly collimated. Since the identification of top-quark and reconstruction of its four momenta will play an important role in our analysis, we make use of the Johns Hopkins (J-H) Top Tagger [76] to identify and reconstruct boosted top-quark initiated jet(s) implemented within the framework of FastJet (version 3.4.0) [77] jet finding and analysis package.

In the boosted top tagging analysis, we consider only those events that have total transverse momentum ( $E_{\text{tot}}$ ) greater than 400 GeV. We use Cambridge-Aachen (C-A) clustering algorithm [78] to define a fat jet with jet radius ( $R$ ) having values in accordance with the  $E_{\text{tot}}$  of these events and these are tabulated in Table IV. The jets thus obtained are then sorted in decreasing order of their transverse momentum. The J-H top tagger iteratively declusters a C-A clustered jet to find the substructure inside a fat jet of radius  $R$ .

The J-H top tagging algorithm requires the specification of the following additional parameters: the fraction of the jet  $p_T$  carried by a subjet and the Manhattan distance (defined as  $|\Delta\eta| + |\Delta\phi|$ ) between two subjets to satisfy minimum values,  $\delta p$  and  $\delta r$ , respectively to be considered as hard and resolved. We tabulate the values of  $R$ ,  $\delta p$  and  $\delta r$  for different total transverse energy of an event,  $E_{\text{tot}}$  in Table IV.

The efficiency of tagging a true top quark initiated jet in the  $p_T$  range 400–1000 GeV is found to be 25%–50% and corresponding light quark/gluon initiated jet being tagged as a top is found to be in the range 0.5%–1.5% in the same range.

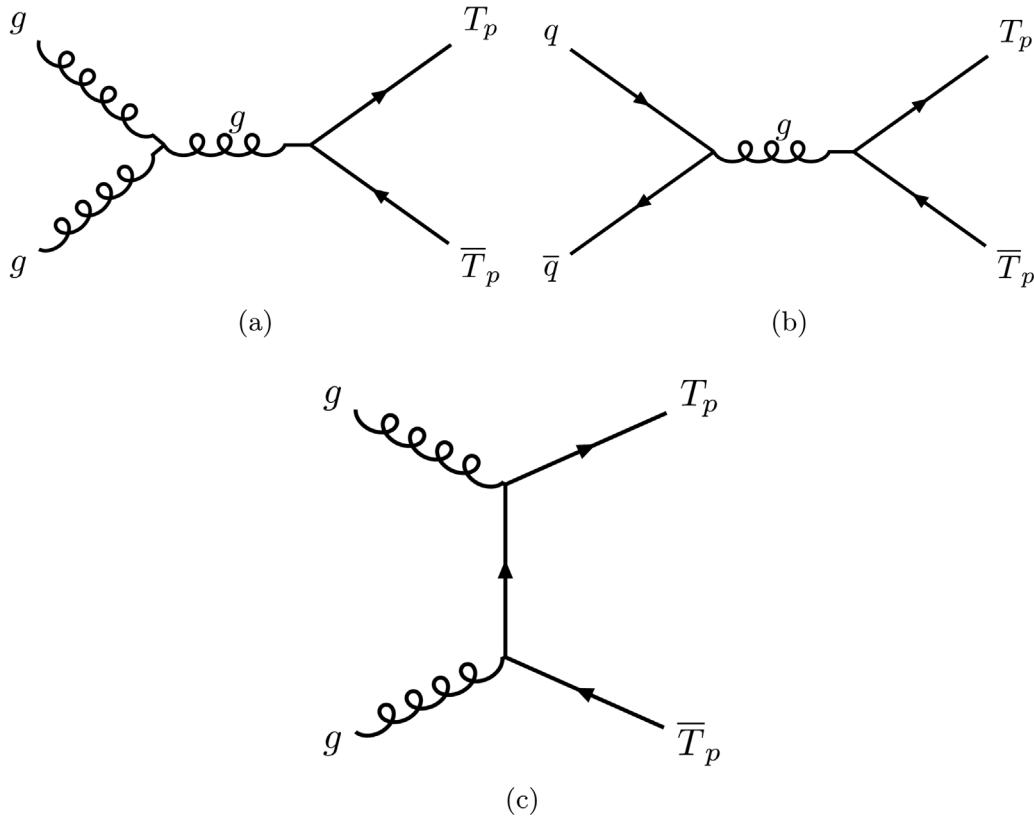


FIG. 4. Feynman diagrams for the pair production of top partner at the LHC.

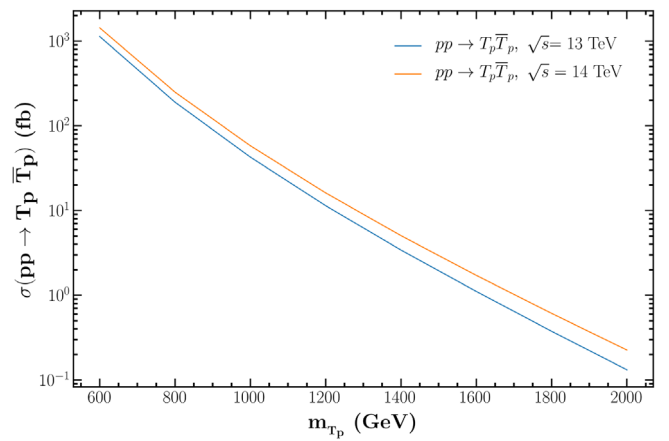
### A. Pair production of top partner

The pair production of top partner at the LHC is dominated by strong production and it depends on the strong coupling constant ( $\alpha_S$ ), the mass of the top partner ( $m_{T_p}$ ) and its spin. This channel is less model dependent, i.e., the production cross section is independent of the details of the model parameters other than the top partner mass. The relevant Feynman diagrams for this process are depicted in Fig. 4. The production cross section as a function of  $m_{T_p}$  is presented in Fig. 5 for 13 and 14 TeV LHC centre of mass energies. The NNLO corrected cross sections at  $\sqrt{s} = 13$  TeV are quoted from [79]. We also use these NNLO corrected cross sections at  $\sqrt{s} = 13$  TeV to extract the  $m_{T_p}$  dependent  $k$ -factors by comparing them to the LO cross sections obtained from MADGRAPH5\_AMC@NLO at the same center of mass energy. These  $k$ -factors are then used to get the NNLO corrected cross section at  $\sqrt{s} = 14$  TeV from the LO cross section provided by Madgraph5\_AMC@NLO at this center of mass energy.

The top partner thus produced further decays substantially to a top quark and a dark photon in this model. So the final state consists of a  $t\bar{t}$  pair and a pair of invisible dark photons ( $pp \rightarrow T_p\bar{T}_p \rightarrow t\bar{t} + 2\gamma_d$ ). The schematic diagram for the same is shown in Fig. 6.

The presence of dark photons in the final state gives rise to missing transverse energy signature as it goes undetected at the detector for the reasons already mentioned in previous sections.

Since the top quark produced in the decay of the top partner are highly boosted we have considered fully hadronic decays of the top quark to implement the boosted


 FIG. 5.  $pp \rightarrow T_p\bar{T}_p$  cross section as a function of the top partner mass at  $\sqrt{s} = 13$  and 14 TeV. [ $\alpha_S(m_Z) = 0.1179$  [63] is used to estimate above cross section].

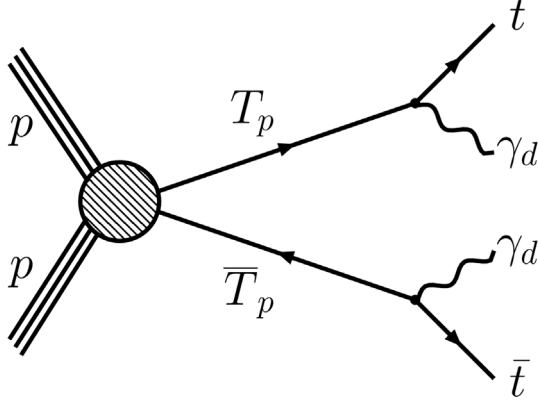


FIG. 6. Schematic diagram for the signal process  $pp \rightarrow T_p \bar{T}_p$  and further decay of  $T_p \rightarrow t \gamma_d$ .

top tagging algorithm efficiently. The final state thus consists of *jets + missing transverse energy* with additional top structure present in it. We require *at least two* central jets with  $p_T > 20$  GeV,  $|\eta| < 2.5$  and no isolated leptons. The SM backgrounds that contribute to such a final state are  $\bar{t}\bar{t}$ ,  $\bar{t}\bar{t}V$  (where  $V = Z/W$ ),  $tW$ , and QCD multijet processes. Since our final state requirement is *at least one* boosted top quark jet, SM  $tj$  process in principle constitutes a potential background. However, the contribution from this background can be eliminated after further event selection criteria that we discuss later. We have listed the SM backgrounds relevant for the pair production analysis in Table V along with their cross sections.

The cross sections quoted in Table V are beyond leading order<sup>7</sup> except for the QCD multijet background which is at leading order. For the simulation of QCD multijet background we have generated  $pp \rightarrow 2j, 3j, 4j$  samples using Madgraph5\_AMC@NLO and interfaced with PYTHIA 8.3 to implement jet parton matching using the MLM matching scheme [83].

### 1. Event selection criteria

We require the final state to have *at least one* boosted top quark jet. If the event contains *exactly one* tagged top quark jet, we take the untagged one of the two hardest jets as a top candidate. We have compared the significances for the two different categories: i.e., requiring *exactly two* boosted top quarks vs *at least one* boosted top quark requirement. It is the later one which gives better significance because of higher signal acceptance ratio. In addition, the kinematic variables we have used later in our analysis (for example, transverse mass ( $M_{T_2}$ ) variable) capture the topology of an event where the top partners are pair produced and decay to semi-invisible mode.

<sup>7</sup>In this analysis the  $\bar{t}\bar{t}$  and  $tW$  is considered at aN<sup>3</sup>LO and  $\bar{t}\bar{t}Z$ ,  $\bar{t}\bar{t}W$  are considered at NLO + NNLL in QCD.

TABLE V. Cross sections of the background processes considered for the top partner pair production analysis at  $\sqrt{s} = 13$  and 14 TeV.

Process	Cross section (fb)	
	13 TeV	14 TeV
$pp \rightarrow \bar{t}\bar{t}$	$8.39 \times 10^5$ [80]	$9.9 \times 10^5$ [80]
$pp \rightarrow \bar{t}\bar{t}Z$	$8.63 \times 10^2$ [81]	$1.045 \times 10^3$ [81]
$pp \rightarrow \bar{t}\bar{t}W$	$5.66 \times 10^2$ [81]	$6.53 \times 10^2$ [81]
$pp \rightarrow tW$	$7.95 \times 10^4$ [82]	$9.4 \times 10^4$ [82]
$pp \rightarrow$ QCD multijet	$1.96 \times 10^{11}$	$2.16 \times 10^{11}$

We propose several kinematic observables including  $M_{T_2}$  which can be useful to efficiently discriminate the signal from the SM backgrounds. Below, we define these variables and present their corresponding distributions.

- (i) Transverse momentum ( $p_T$ ): The transverse momentum of a particle is defined as,

$$p_T = \sqrt{p_x^2 + p_y^2} \quad (19)$$

and corresponding transverse momentum distribution of the tagged top quark jet for both the signal benchmark points and SM backgrounds are shown in Fig. 7.

- (ii) Missing transverse energy ( $\cancel{E}_T$ ): The missing transverse energy is associated with the particles which go undetected at the detector. In a hadronic collider such as the LHC one can use the momentum conservation in the transverse plane to find the transverse components of the total missing momentum associated with all the invisible particles

$$\vec{\cancel{p}}_T = - \sum_{i \in \text{invisible}} \vec{p}_T^i \quad (20)$$

The missing transverse energy is then simply,  $\cancel{E}_T = |\vec{\cancel{p}}_T|$ . Corresponding distributions for both the signal benchmark points and SM backgrounds are shown in Fig. 8.

- (iii) Stranverse mass ( $M_{T_2}$ ): When a heavy particle is pair produced and subsequently decays to a mode which contains both visible as well as a invisible particles in such a situation the final state contains at least two invisible particles coming from both end of the two decay chains (see Fig. 6). The transverse mass variable ( $M_T$ ) defined as

$$M_T = \sqrt{(E_{T,\text{vis}} + \cancel{E}_T)^2 - (\vec{p}_{T,\text{vis}} + \vec{\cancel{p}}_T)^2} \quad (21)$$

is not useful since it will be difficult to reconstruct the missing momentum carried by the individual invisible particle. In this case, one can then make use of the transverse mass variable [84] defined as

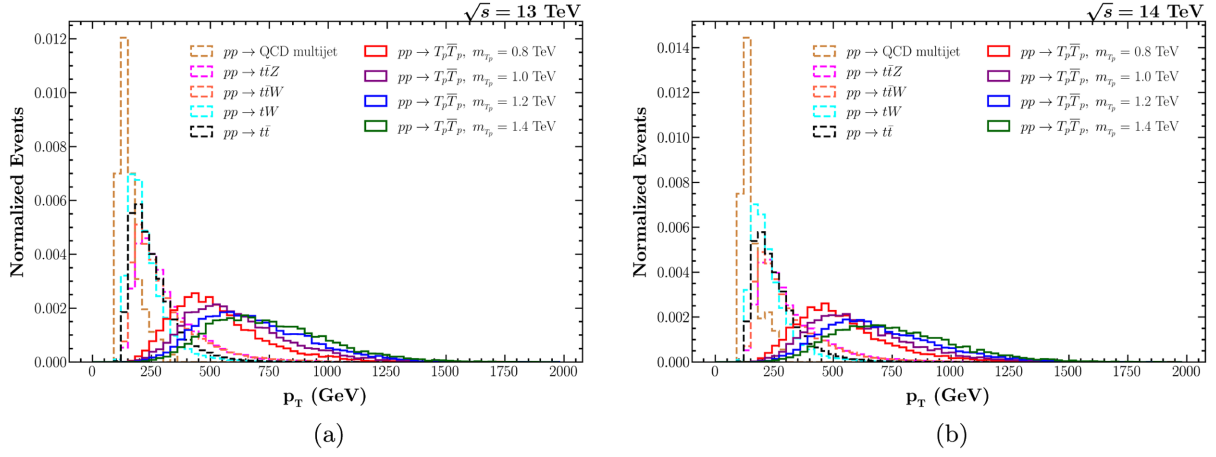


FIG. 7. Transverse momentum ( $p_T$ ) distributions of leading (or only) tagged top quark jet for various signal benchmark points and background processes at 13 and 14 TeV center of mass energies.

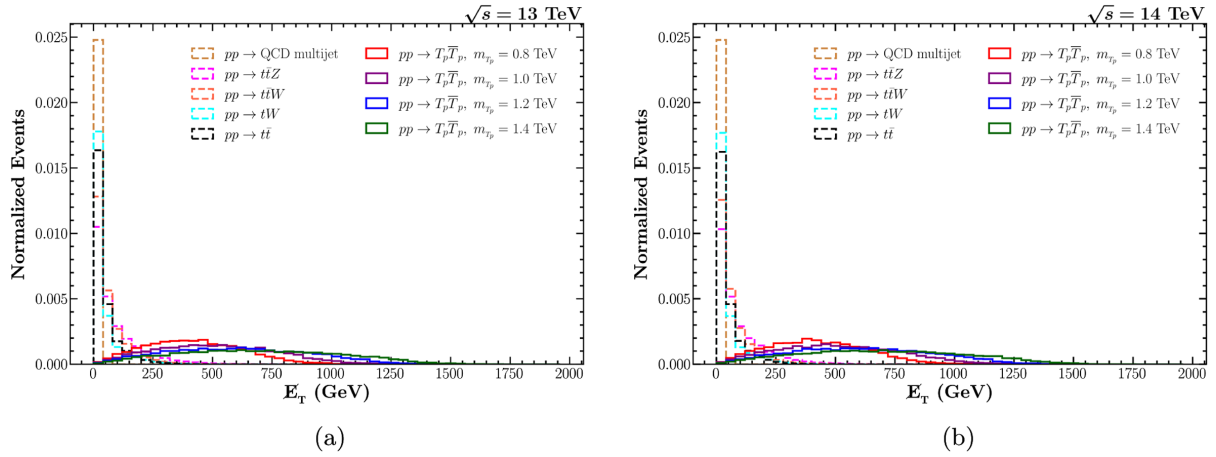


FIG. 8. Distribution of missing transverse energy ( $E_T$ ) variable for signal (top partner pair production) and background processes at 13 and 14 TeV center of mass energies.

$$M_{T2}^2 = \min_{\vec{p}'_1 + \vec{p}'_2 = \vec{p}'_T} \{ \max [ M_T^2(\vec{p}_{1,\text{vis}}, \vec{p}'_1) + M_T^2(\vec{p}_{2,\text{vis}}, \vec{p}'_2) ] \} \leq m_{T_p}^2 \quad (22)$$

where  $\vec{p}_{1,\text{vis}}$  and  $\vec{p}_{2,\text{vis}}$  represent the momenta of the reconstructed top-jets originated in the two decay chains as shown in Fig. 6. The corresponding  $M_{T2}$  distributions for signal benchmark points and backgrounds are shown in Fig. 9.

All these variables play a crucial role in separating the signal from the SM backgrounds quite efficiently as evident from the respective distributions. The optimized event selection criteria<sup>8</sup> are summarized in Table VI after comparing the

<sup>8</sup>The choice of benchmark point dependent cuts can be justified by the fact that the endpoint of transverse mass distribution contains the information about the mass of the top partner.

kinematic distributions for various signal benchmark points and the corresponding SM backgrounds.

## B. Single production of top partner

The single production of top partner in association with a light-quark jet occurs via  $t$ -channel  $W$  boson exchange and requires the presence of  $b$ -quark Parton Distribution Function (PDF) in the five flavor PDF scheme [85]. The relevant Feynman diagrams for this process are shown in Fig. 10. Since the top partner is  $SU(2)_L$  singlet, the single production cross section depends on the mixing of the top-quark with the top partner, parametrized by the mixing angle  $\sin \theta_L$ . The  $T_p - b - W$  coupling being proportional to the mixing angle  $\sin \theta_L$ , the single top partner production cross section is proportional to  $\sin^2 \theta_L$ . Figure 11 depicts the  $\sigma(pp \rightarrow T_p j)$  as a function of the top partner mass ( $m_{T_p}$ ) at 13 and 14 TeV LHC center of mass energies assuming  $\sin \theta_L = 0.1$ . In this case the cross sections are quoted at leading order (LO) using Madgraph\_AMC@NLO.

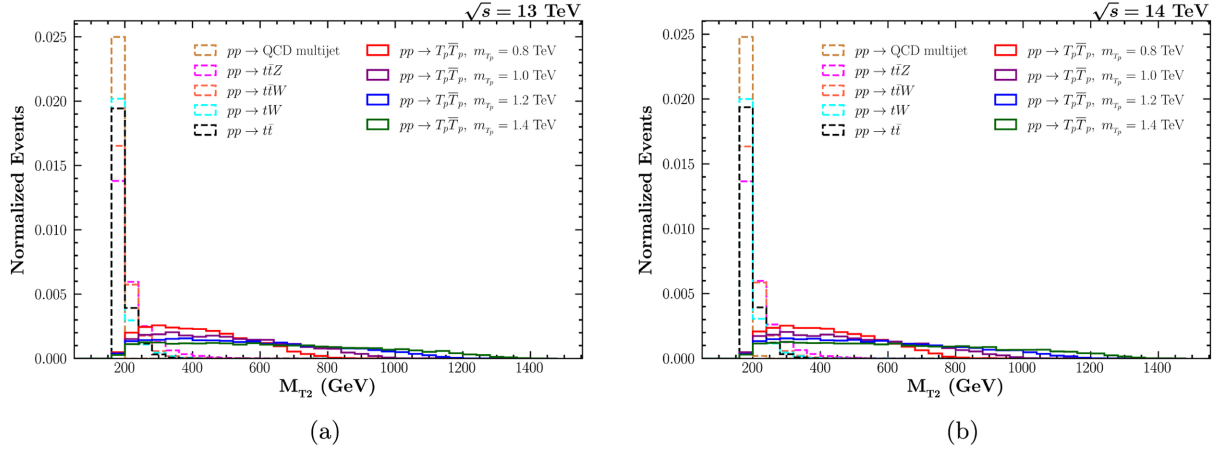


FIG. 9. Distribution of transverse mass ( $M_{T2}$ ) variable for signal (top partner pair production) and background processes at 13 and 14 TeV center of mass energies.

The top partner produced in  $pp$  collision further decays into a top-quark and a dark photon ( $T_p \rightarrow t\gamma_d$ ). Thus giving rise to  $t + \cancel{E}_T + \text{jet}$  final state. Fig. 12 represents a schematic diagram for  $pp \rightarrow T_p \bar{T}_p \rightarrow t\gamma_d j$  process. In this analysis the fully hadronic decay of the top-quark has been considered for the same reason as that in the previous section. We also require the final state to have *at least two* central jets with  $p_T > 20$  GeV,  $|\eta| < 2.5$  and no isolated leptons.

The relevant SM backgrounds in this case are  $t\bar{t}$ ,  $t\bar{t}V$  (where  $V = Z/W$ ),  $tW$ ,  $tj$  and QCD multijet processes. The dominant contribution comes from the  $t\bar{t}$  process and to some extent QCD multijet process given their overwhelming production rate at the LHC. The process  $pp \rightarrow tZj$  with  $Z \rightarrow \bar{\nu}\nu$  constitutes an irreducible background, however, we have estimated its contribution to be negligible and hence, not considered in the following discussion. In Table VII we list these background processes along with their cross sections.

The cross sections quoted in Table VII are beyond leading order<sup>9</sup> except for the QCD multijet background which is at leading order.

### 1. Event selection criteria

In the context of collider simulation of the single top partner production in  $pp$  collision we require the final state to have *exactly one* boosted top quark jet. Furthermore, we again propose certain kinematical variables that can discriminate between the signal and the SM backgrounds. Some of these variables are already defined in the context of pair production of top partner in  $pp$  collision (see Sec. III A) such as transverse momentum ( $p_T$ ) of the reconstructed top and missing transverse energy ( $\cancel{E}_T$ ) will be useful in this analysis as well.

<sup>9</sup>In this analysis the  $t\bar{t}$ ,  $tW$  and  $tj$  are considered at  $\text{aN}^3\text{LO}$  in QCD.

However, instead of the transverse mass variable used in the previous analysis we will use the transverse mass variable ( $M_T$ ) itself as the final state in this case contain only one invisible particle barring the neutrinos from the decay of the top-quarks.

We also use an additional forward jet rapidity cut ( $|\eta| > 2.1$ ) where the forward jet is defined as the maximum rapidity jet which is not tagged as a top quark initiated jet. Figures 13–15 display the distributions of  $p_T$  of the top quark,  $\cancel{E}_T$ , and  $M_T$  of the top quark and the invisible system.

- (i) Transverse momentum ( $p_T$ ):
- (ii) Missing transverse energy ( $\cancel{E}_T$ ):
- (iii) Transverse mass ( $M_T$ ):

The transverse mass  $M_T$  of the reconstructed top quark jet and the missing momentum system following the definition in Eq. (21) is given by,

$$M_T = \sqrt{(E_{T,t} + \cancel{E}_T)^2 - (\vec{p}_{T,t} + \vec{p}_T)^2} \leq m_{T_p} \quad (23)$$

where  $E_{T,t}$  and  $\vec{p}_{T,t}$  represent the reconstructed energy and momentum of the top-jet, respectively.

TABLE VI. Minimum values of the observables  $M_{T2}$ ,  $p_T$ , and  $\cancel{E}_T$  in the context of  $pp \rightarrow T_p \bar{T}_p$  analysis at  $\sqrt{s} = 13$  and 14 TeV.

Minimum values	13 TeV	14 TeV
$M_{T2_0}$	467 ( $m_{T_p} < 1000$ ) 523 ( $m_{T_p} \geq 1000$ )	472
$p_{T_0}$	300	300
$\cancel{E}_{T_0}$	463 ( $m_{T_p} < 1000$ ) 663 ( $m_{T_p} \geq 1000$ )	$0.674 \times m_{T_p}$ ( $m_{T_p} < 1200$ ) 708 ( $m_{T_p} \geq 1200$ )

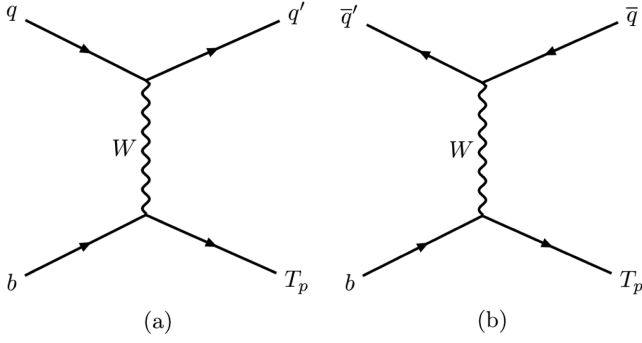


FIG. 10. Feynman diagrams for the single production of top partner at the LHC.

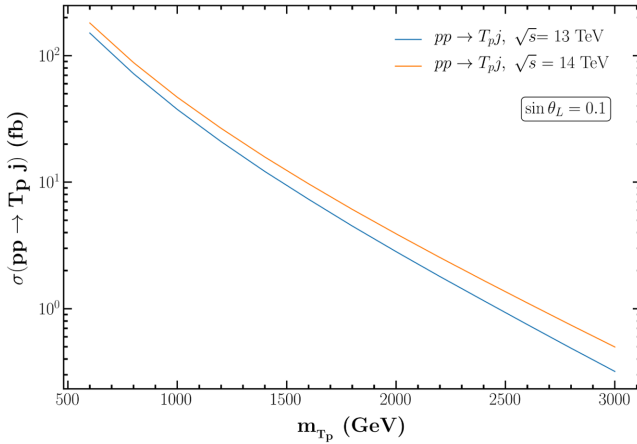


FIG. 11. The cross sections for  $pp \rightarrow T_p j$  process at  $\sqrt{s} = 13$  and 14 TeV respectively, as a function of the top partner mass. [ $\alpha_{EM}^{-1} = 137.036$  [63] is used to estimate the above cross section].

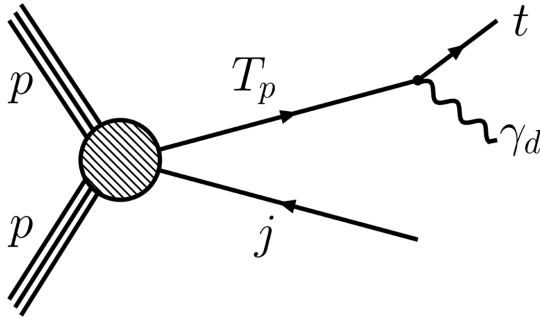


FIG. 12. Schematic diagram for the process  $pp \rightarrow T_p j \rightarrow (T_p \rightarrow t \gamma_d) j$ .

Depending on above distributions, we have imposed the following set of cuts presented in Table VIII, in order to optimize the signal significance.

#### IV. RESULTS AND DISCUSSIONS

In this section, we present the results of our analysis for both the single and pair production of top partner in  $pp$

TABLE VII. Cross sections of the background processes considered for the analysis of single top partner production at  $\sqrt{s} = 13$  and 14 TeV.

Process	Cross section (fb)	
	13 TeV	14 TeV
$pp \rightarrow t\bar{t}$	$8.39 \times 10^5$ [80]	$9.9 \times 10^5$ [80]
$pp \rightarrow t\bar{t}Z$	$8.63 \times 10^2$ [81]	$1.045 \times 10^3$ [81]
$pp \rightarrow t\bar{t}W$	$5.66 \times 10^2$ [81]	$6.53 \times 10^2$ [81]
$pp \rightarrow tW$	$7.95 \times 10^4$ [82]	$9.4 \times 10^4$ [82]
$pp \rightarrow tj$	$1.579 \times 10^5$ [82]	$1.797 \times 10^5$ [82]
$pp \rightarrow \text{QCD multijet}$	$1.96 \times 10^{11}$	$2.16 \times 10^{11}$

collisions at two different LHC center of mass energies (13 and 14 TeV) after implementing the event selection criteria detailed in the previous section for both of these production modes.

#### A. Pair production case

For the top partner pair production process, we consider  $5 \times 10^4$  simulated  $pp \rightarrow T_p \bar{T}_p$  signal events for various choices of the top partner's mass in the range  $\{0.8, 1, 1.2, 1.4, 1.6\}$  TeV against the  $5 \times 10^6$  simulated  $t\bar{t}$ , and  $10^6$  simulated  $tW, t\bar{t}Z, t\bar{t}W$ , and  $1.21 \times 10^6$  QCD multijet background events. Cross sections for each of the background processes are quoted in Table V and the values for  $M_{T_{20}}, p_{T_0}, \cancel{E}_{T_0}$  are given in Table VI.

We illustrate the effects of the cut flow on cross sections for both the signal benchmark points and the estimated total SM background in Table IX and X. The estimated signal significance (defined as  $S/\sqrt{S+B}$ , where  $S$  and  $B$  are the number of signal and background events after applying the hard cuts) at 13 (14) TeV LHC collision energy assuming an integrated luminosity of 139 (300)  $\text{fb}^{-1}$  is also mentioned in Table IX (X).

One can see from Table X that at 14 TeV LHC center of mass energy with 300  $\text{fb}^{-1}$  integrated luminosity it is possible to exclude  $m_{T_p} \leq 1.6$  TeV at  $2\sigma$  significance level. The expected  $2\sigma$  exclusion limits on the  $\sigma(pp \rightarrow T_p \bar{T}_p) \times \text{BR}^2(T_p \rightarrow t \gamma_d)$  for both the  $\sqrt{s} = 13$  and 14 TeV are depicted in Fig. 16. We also depict the constraint coming from the CMS stop searches ( $pp \rightarrow t\bar{t}^*, \bar{t} \rightarrow t\tilde{\chi}_1^0$ ) [53] in the  $t\bar{t}$  + missing transverse energy channel in Fig. 16(a). It is evident that the CMS analysis in this channel gives better limit compared to our analysis in the low  $m_{T_p}$  region and converges near  $m_{T_p} = 1.4$  TeV.

#### B. Single top partner production case

To analyze the  $pp \rightarrow T_p j$  process, we have simulated  $5 \times 10^4$  signal events for top partner mass in the range

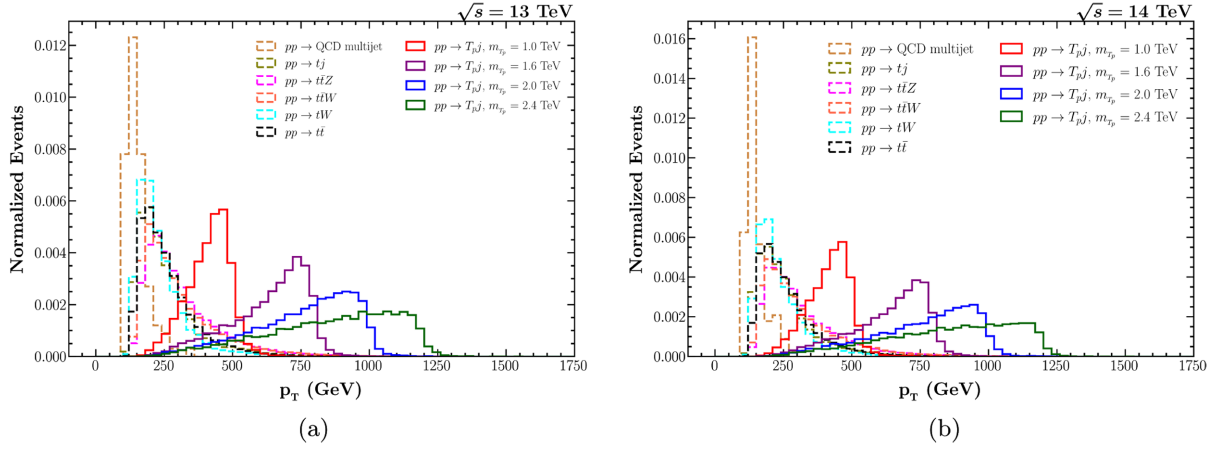


FIG. 13. Transverse momentum ( $p_T$ ) distribution of tagged top quark for signal and background processes at 13 and 14 TeV center of mass energies.

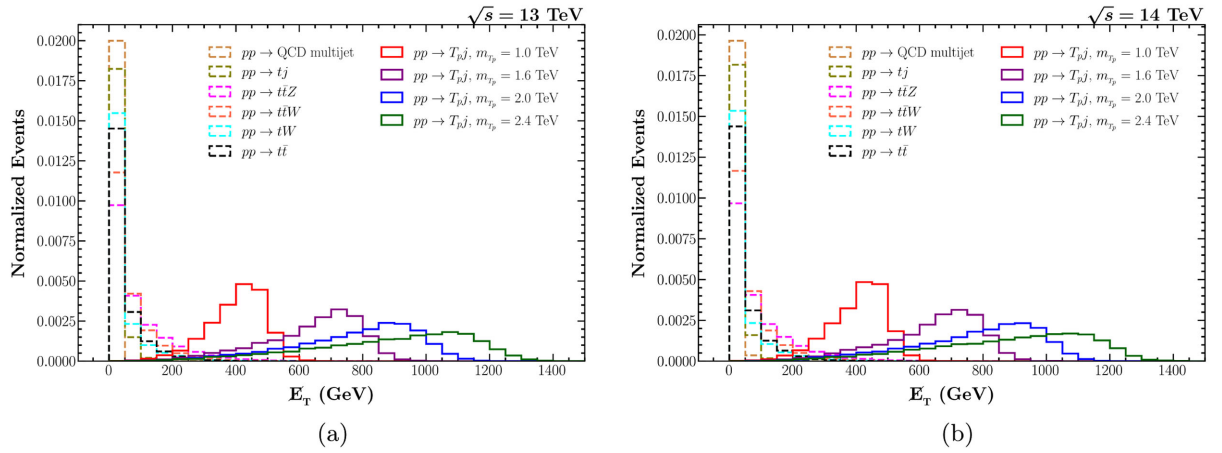


FIG. 14. Distribution of missing transverse energy ( $E_T$ ) variable for signal (single top partner production) and background processes at 13 and 14 TeV center of mass energies.

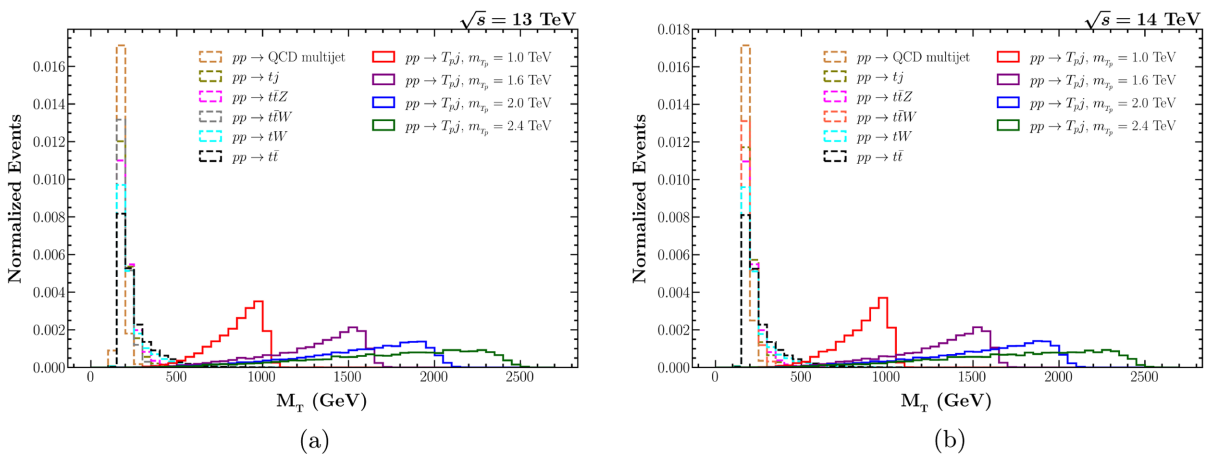


FIG. 15. Distribution of transverse mass ( $M_T$ ) variable for signal (single top partner production) and background processes for 13 and 14 TeV center of mass energies.

TABLE VIII. Minimum values of the observables  $M_T$ ,  $p_T$ , and  $\cancel{E}_T$  in the context of  $pp \rightarrow T_p j$  analysis at  $\sqrt{s} = 13$  and 14 TeV.

Minimum values	13 TeV	14 TeV
$M_{T_0}$	$0.5 \times m_{T_p}$	$0.5 \times m_{T_p}$
$p_{T_0}$	300	300
$\cancel{E}_{T_0}$	$0.40 \times m_{T_p}$ ( $m_{T_p} < 1600$ ) $708$ ( $m_{T_p} \geq 1600$ )	$0.42 \times m_{T_p}$ ( $m_{T_p} < 1800$ ) $774$ ( $m_{T_p} \geq 1800$ )

TABLE IX. Columns [2-7] represent the effects of cut flow on cross sections for both the signal (bold) and the total SM background at  $\sqrt{s} = 13$  TeV.  $\sin \theta_L = 0.1$  is assumed to estimate the branching ratios for the various benchmark choices of  $m_{T_p}$ . The cross sections presented in column [2-7] assume  $\text{BR}(T_p \rightarrow t\gamma_d) = 100\%$ . The estimated signal significance is quoted in the last column assuming *actual* BR (100% BR) with an integrated luminosity of  $139 \text{ fb}^{-1}$ . [ $v_d = 200$  GeV,  $m_{\gamma_d} = 10$  GeV and  $m_{h_d} = 400$  GeV are assumed to obtain the above results].

$m_{T_p}$ (TeV)	Production cross section (fb)	Basic cuts (fb)	Boosted top requirement (fb)	$M_{T_2}$ cut $M_{T_2} > M_{T_{2_0}}$ (fb)	$p_T$ cut $p_T > p_{T_0}$ (fb)	$\cancel{E}_T$ cut $\cancel{E}_T > \cancel{E}_{T_0}$ (fb)	Significance $\left(\frac{S}{\sqrt{S+B}}\right)$
0.8	<b>190.0</b> $1.96 \times 10^{11}$	<b>124.24</b> $7.42 \times 10^{10}$	<b>31.71</b> $1.93 \times 10^7$	<b>11.35</b> 6.14	<b>11.03</b> 5.87	<b>9.86</b> 2.61	16.6 (32.9)
1.0	<b>42.70</b> $1.96 \times 10^{11}$	<b>28.69</b> $7.42 \times 10^{10}$	<b>8.45</b> $1.93 \times 10^7$	<b>3.45</b> 2.48	<b>3.42</b> 2.47	<b>2.15</b> 0.22	8.4 (16.5)
1.2	<b>11.40</b> $1.96 \times 10^{11}$	<b>7.93</b> $7.42 \times 10^{10}$	<b>2.47</b> $1.93 \times 10^7$	<b>1.28</b> 2.48	<b>1.27</b> 2.47	<b>0.96</b> 0.22	4.7 (10.4)
1.4	<b>3.42</b> $1.96 \times 10^{11}$	<b>2.44</b> $7.42 \times 10^{10}$	<b>0.82</b> $1.93 \times 10^7$	<b>0.49</b> 2.48	<b>0.49</b> 2.47	<b>0.40</b> 0.22	2.3 (6.0)
1.6	<b>1.11</b> $1.96 \times 10^{10}$	<b>0.82</b> $7.42 \times 10^{10}$	<b>0.32</b> $1.93 \times 10^7$	<b>0.20</b> 2.48	<b>0.20</b> 2.47	<b>0.17</b> 0.22	1.1 (3.3)

TABLE X. Columns [2-7] represent the effects of cut flow on cross sections for both the signal (bold) and the total SM background at  $\sqrt{s} = 14$  TeV.  $\sin \theta_L = 0.1$  is assumed to estimate the branching ratios for various benchmark choices of  $m_{T_p}$ . The cross sections presented in column [2-7] assume  $\text{BR}(T_p \rightarrow t\gamma_d) = 100\%$ . The estimated signal significance is quoted in the last column assuming *actual* BR (100% BR) with an integrated luminosity of  $300 \text{ fb}^{-1}$ . [ $v_d = 200$  GeV,  $m_{\gamma_d} = 10$  GeV and  $m_{h_d} = 400$  GeV are assumed to obtain the above results].

$m_{T_p}$ (TeV)	Production cross section (fb)	Basic cuts (fb)	Boosted top requirement (fb)	$M_{T_2}$ cut $M_{T_2} > M_{T_{2_0}}$ (fb)	$p_T$ cut $p_T > p_{T_0}$ (fb)	$\cancel{E}_T$ cut $\cancel{E}_T > \cancel{E}_{T_0}$ (fb)	Significance $\left(\frac{S}{\sqrt{S+B}}\right)$
0.8	<b>249.61</b> $2.16 \times 10^{11}$	<b>162.60</b> $8.15 \times 10^{10}$	<b>41.52</b> $2.14 \times 10^7$	<b>14.71</b> 8.55	<b>14.31</b> 8.04	<b>10.06</b> 1.94	26.2 (50.3)
1.0	<b>58.16</b> $2.16 \times 10^{11}$	<b>38.91</b> $8.15 \times 10^{10}$	<b>11.28</b> $2.14 \times 10^7$	<b>5.50</b> 8.55	<b>5.44</b> 8.04	<b>2.90</b> 0.57	13.0 (27.0)
1.2	<b>16.15</b> $2.16 \times 10^{11}$	<b>11.15</b> $8.15 \times 10^{10}$	<b>3.51</b> $2.14 \times 10^7$	<b>2.07</b> 8.55	<b>2.06</b> 8.04	<b>1.25</b> 0.36	7.5 (17.1)
1.4	<b>5.06</b> $2.16 \times 10^{11}$	<b>3.62</b> $8.15 \times 10^{10}$	<b>1.21</b> $2.14 \times 10^7$	<b>0.80</b> 8.55	<b>0.80</b> 8.04	<b>0.57</b> 0.36	3.8 (10.2)
1.6	<b>1.72</b> $2.16 \times 10^{11}$	<b>1.25</b> $8.15 \times 10^{10}$	<b>0.49</b> $2.14 \times 10^7$	<b>0.33</b> 8.55	<b>0.33</b> 8.04	<b>0.26</b> 0.36	1.9 (5.7)

1–2.6 TeV against  $5 \times 10^6$  simulated  $t\bar{t}$ ,<sup>10</sup>  $10^6$  simulated  $tW$ ,  $t\bar{t}Z$ ,  $t\bar{t}W$ ,  $tj$  and  $1.21 \times 10^6$  QCD multijet background events.

<sup>10</sup>For  $m_{T_p} \geq 1.6$  (1.8) TeV, we have simulated  $10^7$   $t\bar{t}$  background events at center of mass energy 13 (14) TeV.

The signal cross sections for various choices of the top partner masses and the effects of various kinematic cuts (listed in Table VIII) for  $\sqrt{s} = 13$  TeV are depicted in Table XI. It also contains the estimated signal significance at 13 TeV LHC collision energy assuming an integrated luminosity of  $139 \text{ fb}^{-1}$ . The results of the corresponding 14 TeV analysis

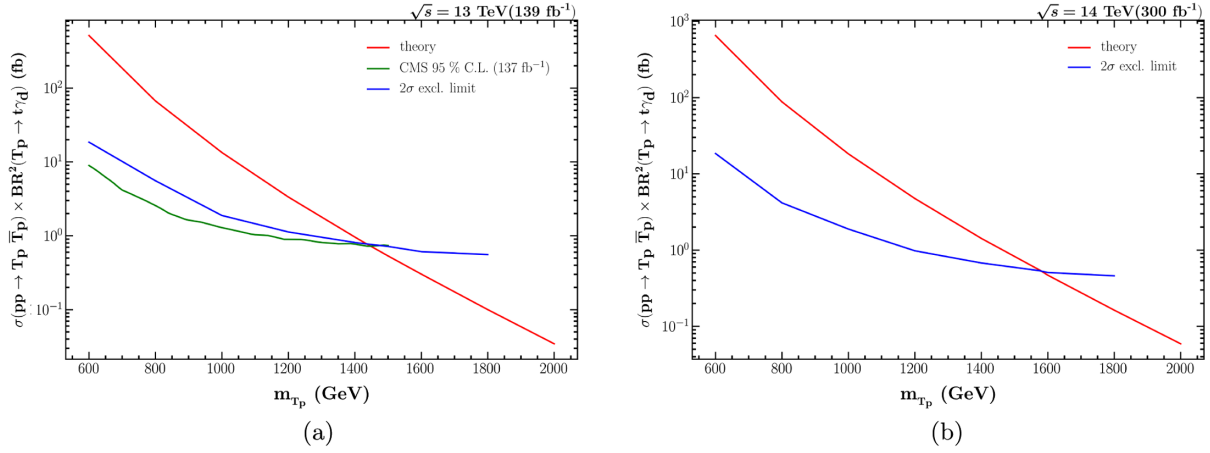


FIG. 16.  $2\sigma$  exclusion limit on the  $\sigma(pp \rightarrow T_p \bar{T}_p) \times \text{BR}^2(T_p \rightarrow t\gamma_d)$  as a function of  $m_{T_p}$  at (a) 13 TeV ( $139 \text{ fb}^{-1}$ ) and (b) 14 TeV ( $300 \text{ fb}^{-1}$ ). [ $\sin\theta_L = 0.1$ ,  $v_d = 200 \text{ GeV}$ ,  $m_{\gamma_d} = 10 \text{ GeV}$  and  $m_{h_d} = 400 \text{ GeV}$  are assumed to obtain the above results].

are depicted in Table XII which contains the signal cross sections, effects of the cut flow on the signal as well as SM background cross sections and the estimated signal significance assuming an integrated luminosity of  $300 \text{ fb}^{-1}$ .

In Table XI (XII), the final background cross sections for  $m_{T_p} > 1.6(1.8) \text{ TeV}$  at  $\sqrt{s} = 13 \text{ TeV}(14 \text{ TeV})$  are all same even though different cross sections are expected as the cuts depend on benchmark point choices. This is visible after the  $M_T$  cut level for  $m_{T_p} > 1.6(1.8) \text{ TeV}$  at  $\sqrt{s} = 13 \text{ TeV}(14 \text{ TeV})$  and also after the  $p_T$  cut level one has the effects of mass dependence in the cross section even

though the  $p_T$  cut is same for these benchmark point. However, after the  $\cancel{E}_T$  cut we have only *two* simulated  $t\bar{t}$  background event left out of  $10^7$  for these benchmark points due to high  $\cancel{E}_T$  cut and a small but nonzero  $t\bar{t}V$  background contribution. This is the reason why the final cross sections are the same for all these benchmark points.

The  $2\sigma$  exclusion limits on  $\sigma(pp \rightarrow T_p j) \times \text{BR}(T_p \rightarrow t\gamma_d)$  in the  $\sin\theta_L - m_{T_p}$  plane for 13 TeV ( $139 \text{ fb}^{-1}$ ) and 14 TeV ( $300 \text{ fb}^{-1}$  and  $3000 \text{ fb}^{-1}$ ) LHC center of mass energies have been presented in Figs. 17(a), 17(b), and 17(c),

TABLE XI. Columns [2-8] depict the effects of cut flow on cross sections for both the signal (bold) and total background at  $\sqrt{s} = 13 \text{ TeV}$ .  $\sin\theta_L = 0.1$  is assumed to estimate the signal cross sections and branching ratios at various benchmark choices of  $m_{T_p}$ . The cross sections presented in column [2-8] assume  $\text{BR}(T_p \rightarrow t\gamma_d) = 100\%$ . The estimated signal significance is quoted in the last column assuming *actual* BR (100% BR) with an integrated luminosity of  $139 \text{ fb}^{-1}$ . [ $v_d = 200 \text{ GeV}$ ,  $m_{\gamma_d} = 10 \text{ GeV}$  and  $m_{h_d} = 400 \text{ GeV}$  are assumed to obtain the above results].

$m_{T_p}$ (TeV)	Production cross section (fb)	Basic cuts (fb)	Boosted top requirement (fb)	$ \eta  > 2.1$	$M_T$ cut $M_T > M_{T_0}$ (fb)	$p_T$ cut $p_T > p_{T_0}$ (fb)	$\cancel{E}_T$ cut $\cancel{E}_T > \cancel{E}_{T_0}$ (fb)	Significance $\left(\frac{S}{\sqrt{S+B}}\right)$
1	<b>37.57</b>	<b>28.38</b>	<b>7.26</b>	<b>6.45</b>	<b>6.30</b>	<b>5.82</b>	<b>3.61</b>	5.2 (9.0)
1.2	$1.96 \times 10^{11}$	$7.42 \times 10^{10}$	$1.81 \times 10^7$	$3.91 \times 10^6$	567.88	427.88	19.04	5.1 (8.8)
1.4	<b>20.92</b>	<b>16.05</b>	<b>4.58</b>	<b>4.12</b>	<b>3.94</b>	<b>3.85</b>	<b>2.35</b>	5.3 (9.0)
1.6	$1.96 \times 10^{11}$	$7.42 \times 10^{10}$	$1.81 \times 10^7$	$3.91 \times 10^6$	254.31	240.55	7.43	5.6 (8.4)
1.8	<b>12.16</b>	<b>9.37</b>	<b>2.89</b>	<b>2.62</b>	<b>2.47</b>	<b>2.46</b>	<b>1.50</b>	5.3 (8.1)
2.0	$1.96 \times 10^{11}$	$7.42 \times 10^{10}$	$1.81 \times 10^7$	$3.91 \times 10^6$	113.26	113.26	2.28	4.1 (6.5)
2.2	<b>7.33</b>	<b>5.65</b>	<b>1.85</b>	<b>1.69</b>	<b>1.56</b>	<b>1.56</b>	<b>0.66</b>	3.0 (4.9)
2.4	$1.96 \times 10^{11}$	$7.42 \times 10^{10}$	$1.81 \times 10^7$	$3.91 \times 10^6$	54.5	54.5	0.19	2.0 (3.4)
	<b>4.50</b>	<b>3.46</b>	<b>1.16</b>	<b>1.06</b>	<b>0.97</b>	<b>0.97</b>	<b>0.62</b>	
	$1.96 \times 10^{11}$	$7.42 \times 10^{10}$	$1.81 \times 10^7$	$3.91 \times 10^6$	27.2	27.2	0.19	
	<b>2.83</b>	<b>2.14</b>	<b>0.71</b>	<b>0.64</b>	<b>0.58</b>	<b>0.58</b>	<b>0.43</b>	
	$1.96 \times 10^{11}$	$7.42 \times 10^{10}$	$1.81 \times 10^7$	$3.91 \times 10^6$	14.6	14.6	0.19	
	<b>1.80</b>	<b>1.34</b>	<b>0.42</b>	<b>0.39</b>	<b>0.34</b>	<b>0.34</b>	<b>0.28</b>	
	$1.96 \times 10^{11}$	$7.42 \times 10^{10}$	$1.81 \times 10^7$	$3.91 \times 10^6$	9.23	9.23	0.19	
	<b>1.16</b>	<b>0.85</b>	<b>0.25</b>	<b>0.23</b>	<b>0.19</b>	<b>0.19</b>	<b>0.17</b>	
	$1.96 \times 10^{11}$	$7.42 \times 10^{10}$	$1.81 \times 10^7$	$3.91 \times 10^6$	5.60	5.60	0.19	

TABLE XII. Columns [2-8] depict the effects of cut flow on cross sections for both the signal (bold) and total background at  $\sqrt{s} = 14$  TeV.  $\sin \theta_L = 0.1$  is assumed to estimate the signal cross sections and branching ratios at various benchmark choices of  $m_{T_p}$ . The cross sections presented in column [2-8] assume  $\text{BR}(T_p \rightarrow t\gamma_d) = 100\%$ . The estimated signal significance is quoted in the last column assuming *actual* BR (100% BR) with an integrated luminosity of  $300 \text{ fb}^{-1}$ . [ $v_d = 200$  GeV,  $m_{\gamma_d} = 10$  GeV and  $m_{h_d} = 400$  GeV are assumed to obtain the above results].

$m_{T_p}$ (TeV)	Production cross section (fb)	Basic cuts (fb)	Boosted top requirement (fb)	$ \eta  > 2.1$	$M_T$ cut $M_T > M_{T_0}$ (fb)	$p_T$ cut $p_T > p_{T_0}$ (fb)	$\cancel{E}_T$ cut $\cancel{E}_T > \cancel{E}_{T_0}$ (fb)	Significance $\left(\frac{S}{\sqrt{S+B}}\right)$
1	<b>46.89</b> $2.16 \times 10^{11}$	<b>35.63</b> $8.17 \times 10^{10}$	<b>9.01</b> $2.00 \times 10^7$	<b>8.07</b> $5.73 \times 10^6$	<b>7.88</b> 713.3	<b>7.35</b> 533.1	<b>3.91</b> 19.2	8.2 (14.1)
1.2	<b>26.65</b> $2.16 \times 10^{11}$	<b>20.46</b> $8.17 \times 10^{10}$	<b>5.85</b> $2.00 \times 10^7$	<b>5.29</b> $5.73 \times 10^6$	<b>5.07</b> 320.5	<b>4.96</b> 303.2	<b>2.56</b> 7.0	8.3 (14.4)
1.4	<b>15.81</b> $2.16 \times 10^{11}$	<b>12.14</b> $8.17 \times 10^{10}$	<b>3.79</b> $2.00 \times 10^7$	<b>3.46</b> $5.73 \times 10^6$	<b>3.25</b> 147.8	<b>3.24</b> 147.7	<b>1.69</b> 3.1	7.8 (13.4)
1.6	<b>9.70</b> $2.16 \times 10^{11}$	<b>7.48</b> $8.17 \times 10^{10}$	<b>2.48</b> $2.00 \times 10^7$	<b>2.26</b> $5.73 \times 10^6$	<b>2.10</b> 73.4	<b>2.10</b> 73.4	<b>1.09</b> 0.95	8.0 (13.2)
1.8	<b>6.09</b> $2.16 \times 10^{11}$	<b>4.67</b> $8.17 \times 10^{10}$	<b>1.56</b> $2.00 \times 10^7$	<b>1.43</b> $5.73 \times 10^6$	<b>1.31</b> 36.2	<b>1.31</b> 36.2	<b>0.60</b> 0.23	7.3 (11.5)
2.0	<b>3.91</b> $2.16 \times 10^{11}$	<b>2.96</b> $8.17 \times 10^{10}$	<b>0.97</b> $2.00 \times 10^7$	<b>0.90</b> $5.73 \times 10^6$	<b>0.80</b> 18.0	<b>0.80</b> 18.0	<b>0.50</b> 0.23	6.4 (10.2)
2.2	<b>2.54</b> $2.16 \times 10^{11}$	<b>1.89</b> $8.17 \times 10^{10}$	<b>0.59</b> $2.00 \times 10^7$	<b>0.54</b> $5.73 \times 10^6$	<b>0.48</b> 10.8	<b>0.48</b> 10.8	<b>0.35</b> 0.23	4.8 (7.9)
2.4	<b>1.67</b> $2.16 \times 10^{11}$	<b>1.22</b> $8.17 \times 10^{10}$	<b>0.36</b> $2.00 \times 10^7$	<b>0.33</b> $5.73 \times 10^6$	<b>0.28</b> 6.53	<b>0.28</b> 6.53	<b>0.22</b> 0.23	3.3 (5.7)
2.5	<b>1.36</b> $2.16 \times 10^{11}$	<b>0.98</b> $8.17 \times 10^{10}$	<b>0.28</b> $2.00 \times 10^7$	<b>0.26</b> $5.73 \times 10^6$	<b>0.22</b> 4.54	<b>0.22</b> 4.54	<b>0.18</b> 0.23	2.7 (4.8)
2.6	<b>1.11</b> $2.16 \times 10^{11}$	<b>0.79</b> $8.17 \times 10^{10}$	<b>0.22</b> $2.00 \times 10^7$	<b>0.20</b> $5.73 \times 10^6$	<b>0.17</b> 3.14	<b>0.17</b> 3.14	<b>0.14</b> 0.23	2.3 (4.1)

respectively, assuming  $v_d = 200$  GeV,  $m_{\gamma_d} = 10$  GeV, and  $m_{h_d} = 400$  GeV.

In these figures, we also depict the constraints coming from various other observations in the  $\sin \theta_L - m_{T_p}$  plane. The most stringent of these constraints is the one coming from the latest LHC data which rules out  $\sin \theta_L > 0.11$  for  $m_{T_p} \leq 1.95$  TeV [54]. However, for  $m_{T_p} \geq 1.95$  TeV the EWP datasets more stringent limit on  $\sin \theta_L$ , which rules out  $\sin \theta_L > 0.11$  in this mass range.

Figure 17(a) shows that the region of parameter space that can be ruled out using ATLAS data [54], namely,  $\sin \theta_L \gtrsim 0.1$  for  $m_{T_p} \gtrsim 2$  TeV is already excluded by the EWP data for the singlet top partner case irrespective of its decay branching ratio. Our analysis at  $\sqrt{s} = 13$  TeV with integrated luminosity of  $139 \text{ fb}^{-1}$  in the single top partner mode gives comparatively better limit in the  $\sin \theta_L - m_{T_p}$  plane.

More importantly, in the high-luminosity phase of the LHC run which will be able to probe even a smaller production cross section corresponding to  $\sin \theta_L \sim 0.03-0.05$  in the mass range  $1.0 \text{ TeV} \lesssim m_{T_p} \lesssim 2.6 \text{ TeV}$ , the analysis we presented here for the single top partner channel will be of much relevance. This is because it is exactly the range of parameter space where the decay width of the top partner in the traditional modes are highly

suppressed compared to the nonstandard modes (see Fig. 2).

In fact, the branching ratio of  $T_p \rightarrow t\gamma_d$  could be as large as 60%–70% (see Fig. 3) depending on the masses of the dark photon and dark Higgs and the choice of  $v_d$ .<sup>11</sup>

The study of the single production of the top partner at the LHC in the single top +  $\cancel{E}_T$  + jet final state and the event selection criteria listed in Sec. III shows if the top partner dominantly decays to a top quark and an invisible dark photon, it will be possible to set potentially stringent limit in the  $\sin \theta_L - m_{T_p}$  plane. We obtained a  $2\sigma$  exclusion limit on  $\sin \theta_L$  as low as  $\sim 0.025$  up to  $m_{T_p} \sim 2.0$  TeV at  $\sqrt{s} = 14$  TeV with  $3 \text{ ab}^{-1}$  integrated luminosity. For  $m_{T_p}$  up to 2.6 TeV  $\sin \theta_L \geq 0.05$  can be excluded at  $2\sigma$  significance with the same specification.

We also present a  $5\sigma$  ( $3\sigma$ ) discovery (exclusion) limit on  $m_{T_p}$  using the single production of top partner analysis as a function of the integrated luminosity at  $\sqrt{s} = 14$  TeV, assuming  $\sin \theta_L = 0.1, 0.05$ . Figure 18 shows that at

<sup>11</sup>For low,  $v_d \sim 1$  GeV the allowed ranges of  $\sin \theta_L$  consistent with the perturbative unitarity bound are so small [ $|\sin \theta_L| \lesssim 0.002$ , see Fig. 1(a)] that it is not sensitive to LHC analyses.

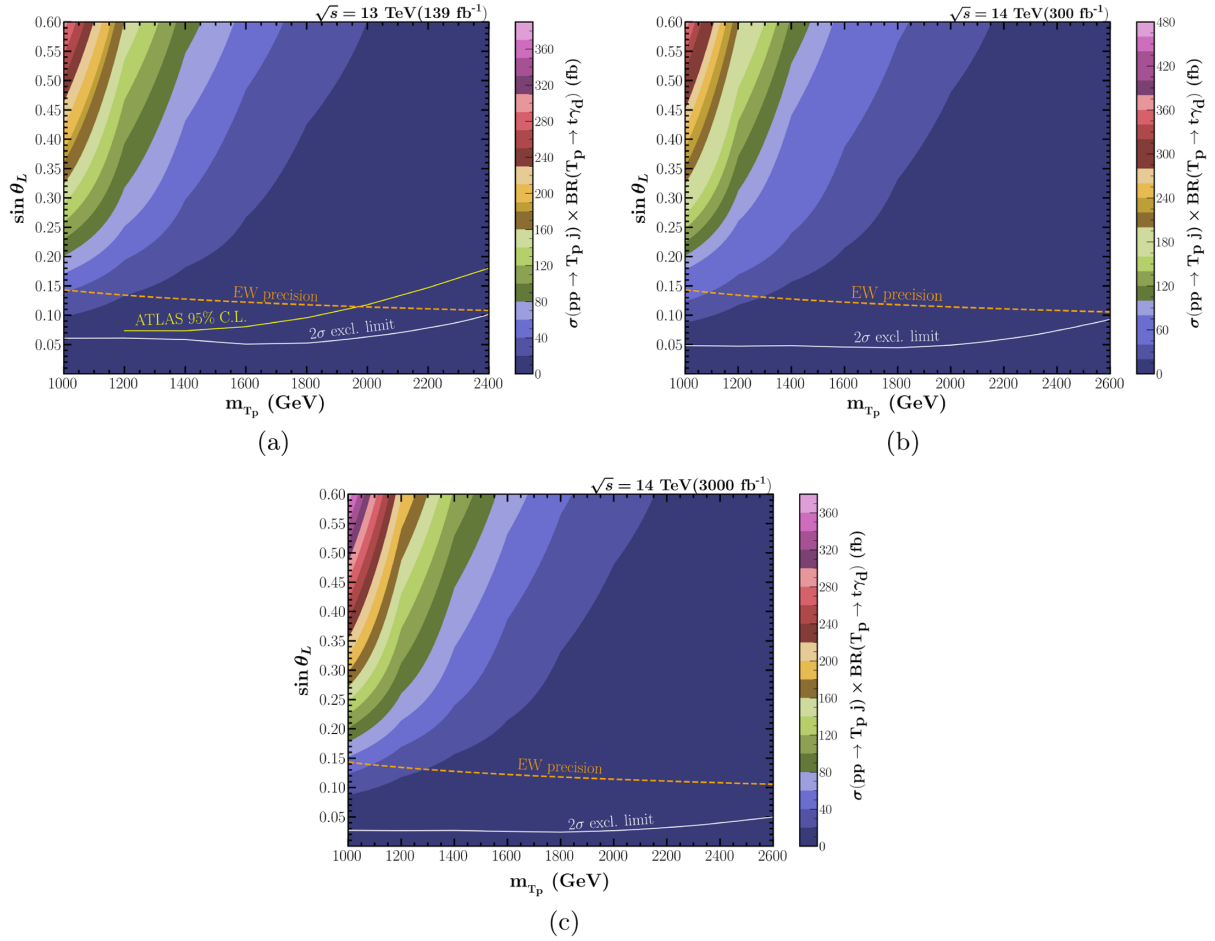


FIG. 17.  $2\sigma$  exclusion limit on  $\sigma(pp \rightarrow T_p j) \times \text{BR}(T_p \rightarrow t\gamma_d)$  in the  $\sin \theta_L - m_{T_p}$  plane at (a) 13 TeV(139 fb<sup>-1</sup>), (b) 14 TeV (300 fb<sup>-1</sup>) and (c) 14 TeV (3000 fb<sup>-1</sup>). [ $v_d = 200$  GeV,  $m_{\gamma_d} = 10$  GeV and  $m_{h_d} = 400$  GeV are assumed to obtain the above results].

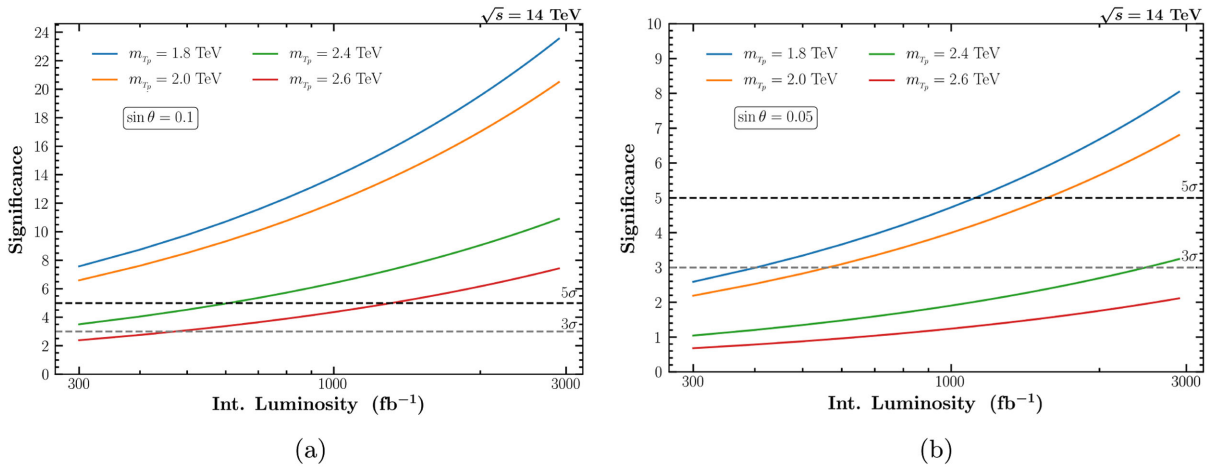


FIG. 18. The LHC reach for  $m_{T_p}$  at  $3\sigma$  and  $5\sigma$  significance level as a function of the integrated luminosity at  $\sqrt{s} = 14$  TeV for two different choices of (a).  $\sin \theta_L = 0.1$  and (b).  $\sin \theta_L = 0.05$ .

$\sqrt{s} = 14$  TeV assuming  $3 \text{ ab}^{-1}$  integrated luminosity one can exclude  $m_{T_p} \leq 2.4$  TeV for  $\sin \theta_L = 0.05$  at  $3\sigma$  significance level.

## V. CONCLUSIONS

We have discussed the phenomenology of a VLQ which is charged under both the SM gauge interaction and also carries an additional dark  $U(1)_d$  charge. This gives rise to some new consequences in terms of its decay. We have shown that in a large region of the parameter space, the top partner predominantly decays to a top and a dark photon/dark Higgs ( $T_p \rightarrow t + \gamma_d/h_d$ ) with its traditional decay modes suppressed. This not only helps one to evade the strong bounds coming from LHC searches for a top partner in the traditional channels such as  $T_p \rightarrow bW, tZ$ , or  $th$  it opens up a new possibility to search for them at the LHC. We have focused on the  $T_p \rightarrow t\gamma_d$  decay mode and analyzed the pair and single production of top partner at the LHC in the  $t\bar{t} + \cancel{E}_T$  and  $t + \cancel{E}_T$  final states, respectively, assuming that the dark photon decays to an invisible system or is stable at the length scale of the detector.

A striking feature of our signal is that the top quark produced in the decay of the top partner is highly boosted and one can use the boosted top tagging technique to reconstruct the momentum of the top quark initiated jet in the hadronic channel. We have proposed several kinematic variables such as transverse momentum of the reconstructed top quark, missing transverse momentum and transverse mass or transverse mass to suppress the dominant SM backgrounds in these channels. We have shown that top partner mass up to 1.6 TeV can be excluded with more than  $2\sigma$  significance using the top-pair production channel. We have also incorporated the limit coming from the LHC analysis for *stop pair searches* [ $pp \rightarrow \tilde{t}\tilde{t}^* \rightarrow (t\tilde{\chi}_1^0)(\tilde{t}\tilde{\chi}_1^0)$ ] in the same final state.

The single production of the top partner is sensitive to the mass of the top partner,  $m_{T_p}$ , and the mixing angle,  $\sin \theta_L$ . The constraints coming from the EWPO and perturbative unitarity mostly prefer a very small mixing angle ( $|\sin \theta_L| \lesssim 0.1$ ). Such a small mixing angle will imply small cross section in the single top partner production case. The future run of LHC at 14 TeV center of mass energy with  $3 \text{ ab}^{-1}$  integrated luminosity will be sensitive to such small mixing angle, i.e.,  $\sin \theta_L \sim 0.05\text{--}0.1$ . For  $m_{T_p} \sim 2.5$  TeV, this is exactly the range consistent with the hierarchy  $|\sin \theta_L| \ll m_t/m_{T_p} \ll 1$ . This is also the case where one has the branching ratio enhancement in the  $t\gamma_d$  and  $th_d$  channels. Using simple cut based analysis we have set an exclusion limit in the  $\sin \theta_L - m_{T_p}$  plane. We have shown that  $\sin \theta_L \sim 0.025$  (0.05) can be ruled out for  $m_{T_p} \leq 2.0$  (2.6) TeV at a 95% confidence level using the future

LHC data corresponding to  $3 \text{ ab}^{-1}$  integrated luminosity and  $\sqrt{s} = 14$  TeV. We have also considered bounds coming from the latest LHC data in the single top partner channel with  $T \rightarrow tZ \rightarrow t(Z \rightarrow \nu\bar{\nu})$ . We have also presented LHC reach for top partner mass as a function of integrated luminosity at 14 TeV center of mass energy. Our collider analysis will also be applicable whenever the top partner decays to a top and an invisible system other than dark photon assuming  $m_{T_p}, \sin \theta_L$  and  $\text{BR}(T_p \rightarrow t + \text{invisible})$  as independent parameters.

## ACKNOWLEDGMENTS

S. B. is thankful to Emidio Gabrielli and Subhadeep Mondal for useful discussions. S. V. is thankful for support provided by Council of Scientific and Industrial Research (CSIR, India) under CSIR-UGC NET Fellowship (File No. : 09/934(0017)/2020-EMR-I). A. C. would like to thank Indian Institute of Technology, Kanpur for supporting this work by means of Institute Post-Doctoral Fellowship (Ref.No. DF/PDF197/2020-IITK/970).

## APPENDIX A: EWPO

For a singlet top partner model, we follow [52] to get the general expression for corrections to oblique parameters and  $Zb\bar{b}$  couplings,

$$\Delta T = \frac{N_c m_t^2}{16\pi \sin_W^2 m_W^2} \sin^2 \theta_L \left[ -(1 + \cos^2 \theta_L) + 2\cos^2 \theta_L \frac{r_T}{r_T - 1} \log(r_T) + r_T \sin^2 \theta_L \right] \quad (\text{A1})$$

$$\Delta S = \frac{N_c}{18\pi} \sin^2 \theta_L \left[ \log(r_T) + \cos^2 \theta_L \left( \frac{5(r_T^2 + 1) - 22r_T}{(1 - r_T)^2} + \frac{3(r_T + 1)(r_T^2 - 4r_T + 1)}{(1 - r_T)^3} \log(r_T) \right) \right] \quad (\text{A2})$$

$$\delta X_{bb}^L = \frac{g^2}{32\pi^2} \sin^2 \theta_L [f_1(x, x') + \cos^2 \theta_L f_2(x, x')] \quad (\text{A3})$$

where,  $r_T = m_{T_p}/m_t$ ,  $x = m_t^2/m_W^2$ ,  $x' = m_{T_p}^2/m_W^2$  and,

$$f_1(x, x') = x' - x + 3 \log\left(\frac{x'}{x}\right) \quad (\text{A4})$$

$$f_2(x, x') = -x' - x + \frac{2x'x}{x' - x} \log\left(\frac{x'}{x}\right) \quad (\text{A5})$$

## APPENDIX B: PARTIAL DECAY WIDTHS

In this section we list the formulas for the decay widths of the top partner in various modes.<sup>12</sup>

### 1. $T_p \rightarrow bW$

$$\mathcal{L}_{T_p-b-W} = \bar{T}_p \gamma^\mu (V_L P_L) b W_\mu + \text{H.c.} \quad (\text{B1})$$

The exact model independent expression for  $\Gamma(T_p \rightarrow bW)$  is given by

$$\begin{aligned} \Gamma(T_p \rightarrow bW) &= \frac{1}{16\pi} \frac{m_{T_p}^3}{m_W^2} \lambda^{1/2} \left( 1, \frac{m_b^2}{m_{T_p}^2}, \frac{m_W^2}{m_{T_p}^2} \right) \\ &\left[ \left( 1 - \frac{m_b^2}{m_{T_p}^2} \right)^2 + \frac{m_W^2}{m_{T_p}^2} - 2 \frac{m_W^4}{m_{T_p}^4} + \frac{m_W^2 m_b^2}{m_{T_p}^2} \right] \\ &\times \left( \frac{|V_L^2|}{2} \right) \end{aligned} \quad (\text{B2})$$

where,

$$\lambda(a, b, c) = a^2 + b^2 + c^2 - 2ab - 2bc - 2ca \quad (\text{B3})$$

In the present model, we have

$$V_L = \frac{g \sin \theta_L}{\sqrt{2}} \quad (\text{B4})$$

In the limit  $|\sin \theta_d|, |\sin \theta_S|, \varepsilon, m_t/m_{T_p} \ll 1$  Eq. (B2) reduces to

$$\Gamma(T_p \rightarrow bW) \approx \frac{1}{16\pi} \frac{m_{T_p}^3}{v_{EW}^2} \sin^2 \theta_L \quad (\text{B5})$$

### 2. $T_p \rightarrow tV$

$$\mathcal{L}_{T_p-t-V} = -\bar{T}_p \gamma^\mu (V_L P_L + V_R P_R) t V_\mu + \text{H.c.} \quad (\text{B6})$$

The exact model independent expression for  $\Gamma(T_p \rightarrow tV)$  is given by

$$\begin{aligned} \Gamma(T_p \rightarrow tV) &= \frac{1}{16\pi} \frac{m_{T_p}^3}{m_V^2} \lambda^{1/2} \left( 1, \frac{m_t^2}{m_{T_p}^2}, \frac{m_V^2}{m_{T_p}^2} \right) \\ &\left\{ \left[ \left( 1 - \frac{m_t^2}{m_{T_p}^2} \right)^2 + \frac{m_V^2}{m_{T_p}^2} - 2 \frac{m_V^4}{m_{T_p}^4} + \frac{m_V^2 m_t^2}{m_{T_p}^2} \right] \right. \\ &\times \left( \frac{|V_L^2| + |V_R^2|}{2} \right) \\ &\left. - 3 \frac{m_t}{m_{T_p}} \frac{m_V^2}{m_{T_p}^2} (V_L V_R^* + V_L^* V_R) \right\} \end{aligned} \quad (\text{B7})$$

In this model, for  $V = Z$ , we have

$$V_L = \frac{1}{4} \sin 2\theta_L [\hat{g}_Z (\cos \theta_d + \sin \theta_d \hat{t}_W \varepsilon) + 2g_d \sin \theta_d] \quad (\text{B8})$$

$$\begin{aligned} V_R &= \frac{1}{2} g_d \sin \theta_d \sin 2\theta_R \\ &= \frac{1}{2} g_d \sin \theta_d \sin 2\theta_L \frac{m_{T_p} m_t}{m_t^2 \cos^2 \theta_L + m_{T_p}^2 \sin^2 \theta_L} \end{aligned} \quad (\text{B9})$$

and for  $V = \gamma_d$ , we have

$$V_L = \frac{1}{4} \sin 2\theta_L [\hat{g}_Z (\sin \theta_d - \cos \theta_d \hat{t}_W \varepsilon) - 2g_d \cos \theta_d] \quad (\text{B10})$$

$$\begin{aligned} V_R &= -\frac{1}{2} g_d \cos \theta_d \sin 2\theta_R \\ &= -\frac{1}{2} g_d \cos \theta_d \sin 2\theta_L \frac{m_{T_p} m_t}{m_t^2 \cos^2 \theta_L + m_{T_p}^2 \sin^2 \theta_L} \end{aligned} \quad (\text{B11})$$

where  $\theta_d$  is the mixing angle between the Abelian gauge bosons.

$$\hat{t}_W = \frac{\sin \hat{\theta}_W}{\cos \hat{\theta}_W} \quad (\text{B12})$$

$$\sin \hat{\theta}_W = \sin \theta_W + \mathcal{O}(\varepsilon^2) \quad (\text{B13})$$

$$\hat{g}_Z = \frac{g}{\cos \hat{\theta}_W} \quad (\text{B14})$$

$$g_d = \frac{m_{\gamma_d}}{v_d} + \mathcal{O}(\varepsilon^2) \quad (\text{B15})$$

$$g_d = \frac{g'_d}{\sqrt{1 - (\varepsilon^2 / \cos^2 \hat{\theta}_W)}} \quad (\text{B16})$$

In the limit  $|\sin \theta_d|, |\sin \theta_S|, \varepsilon, m_t/m_{T_p} \ll 1$  Eq. (B7) simplifies to the following two equations for  $V = Z$  and  $\gamma_d$

$$\Gamma(T_p \rightarrow tZ) \approx \frac{1}{32\pi} \frac{m_{T_p}^3}{v_{EW}^2} \sin^2 \theta_L \cos^2 \theta_L \quad (\text{B17})$$

<sup>12</sup>We have calculated both the general and model specific expressions for the decay widths independently. The general expressions for the decay widths agree with Refs. [12,13] in various special cases or limits.

and,

$$\Gamma(T_p \rightarrow t\gamma_d) \approx \frac{1}{32\pi} \frac{m_{T_p}^3}{v_d^2} \sin^2\theta_L \cos^2\theta_L \times \left(1 + \frac{m_{T_p}^2 m_t^2}{D^2}\right) \quad (\text{B18})$$

where,  $D = m_t^2 \cos^2\theta_L + m_{T_p}^2 \sin^2\theta_L$ .

### 3. $T_p \rightarrow tS$

$$\mathcal{L}_{T_p-tS} = -\bar{T}_p(Y_L P_L + Y_R P_R)tS + \text{H.c.} \quad (\text{B19})$$

The exact model independent expression for  $\Gamma(T_p \rightarrow tS)$  is given by

$$\begin{aligned} \Gamma(T_p \rightarrow tS) = \frac{1}{16\pi} m_{T_p} \lambda^{1/2} & \left(1, \frac{m_t^2}{m_{T_p}^2}, \frac{m_S^2}{m_{T_p}^2}\right) \\ & \left\{ \left[1 + \frac{m_t^2}{m_{T_p}^2} - \frac{m_S^2}{m_{T_p}^2}\right] \left(\frac{|Y_L^2| + |Y_R^2|}{2}\right) \right. \\ & \left. + \frac{m_t}{m_{T_p}} (Y_L Y_R^* + Y_L^* Y_R) \right\} \quad (\text{B20}) \end{aligned}$$

In this model, for  $S = h$

$$Y_L = \frac{1}{\sqrt{2}} \sin\theta_R (y_t \cos\theta_L \cos\theta_S + \lambda_T \sin\theta_L \sin\theta_S) \quad (\text{B21})$$

$$Y_R = \frac{1}{\sqrt{2}} \cos\theta_R (y_t \sin\theta_L \cos\theta_S - \lambda_T \cos\theta_L \sin\theta_S) \quad (\text{B22})$$

and for  $S = h_d$

$$Y_L = \frac{1}{\sqrt{2}} \sin\theta_R (y_t \cos\theta_L \sin\theta_S - \lambda_T \sin\theta_L \cos\theta_S) \quad (\text{B23})$$

$$Y_R = \frac{1}{\sqrt{2}} \cos\theta_R (y_t \sin\theta_L \sin\theta_S + \lambda_T \cos\theta_L \cos\theta_S) \quad (\text{B24})$$

where

$$y_t = \sqrt{2} \frac{\sqrt{m_t^2 \cos^2\theta_L + m_{T_p}^2 \sin^2\theta_L}}{v_{\text{EW}}} \quad (\text{B25})$$

$$\lambda_T = \frac{(m_{T_p}^2 - m_t^2) \sin 2\theta_L}{\sqrt{2} v_d \sqrt{m_t^2 \cos^2\theta_L + m_{T_p}^2 \sin^2\theta_L}} \quad (\text{B26})$$

$$m_T = \frac{m_t m_{T_p}}{\sqrt{m_t^2 \cos^2\theta_L + m_{T_p}^2 \sin^2\theta_L}} \quad (\text{B27})$$

$$\sin\theta_R = \frac{m_T}{m_t} \sin\theta_L \quad (\text{B28})$$

$$\cos\theta_R = \frac{m_T}{m_{T_p}} \cos\theta_L \quad (\text{B29})$$

and  $\theta_S$  is a mixing angle in the scalar sector.

In the limit  $|\sin\theta_d|, |\sin\theta_S|, \varepsilon, m_t/m_{T_p} \ll 1$  Eq. (B20) simplifies to the following two equations for  $S = h$  and  $h_d$

$$\Gamma(T_p \rightarrow th) \approx \frac{1}{32\pi} \frac{m_{T_p}^3}{v_{\text{EW}}^2} \sin^2\theta_L \cos^2\theta_L \quad (\text{B30})$$

and,

$$\begin{aligned} \Gamma(T_p \rightarrow th_d) \approx \frac{1}{32\pi} \frac{m_{T_p}^3}{v_d^2} \sin^2\theta_L \cos^2\theta_L \\ \times \frac{m_{T_p}^4}{D^2} \left( \sin^4\theta_L + \frac{m_t^2}{m_{T_p}^2} \cos^4\theta_L \right. \\ \left. + 4 \frac{m_t^2}{m_{T_p}^2} \sin^2\theta_L \cos^2\theta_L \right) \quad (\text{B31}) \end{aligned}$$

- 
- [1] B. C. Allanchach, Beyond the standard model, *CERN Yellow Rep. School Proc.* **6**, 113 (2019).  
 [2] L. Randall and R. Sundrum, Large Mass Hierarchy from a Small Extra Dimension, *Phys. Rev. Lett.* **83**, 3370 (1999).  
 [3] M. Carena, E. Ponton, J. Santiago, and C. E. M. Wagner, Electroweak constraints on warped models with custodial symmetry, *Phys. Rev. D* **76**, 035006 (2007).  
 [4] R. S. Chivukula, Lectures on technicolor and compositeness, in *Theoretical Advanced Study Institute in Elementary*

*Particle Physics (TASI 2000): Flavor Physics for the Millennium*, pp. 731–772, 6, 2000.

- [5] D. B. Kaplan, H. Georgi, and S. Dimopoulos, Composite Higgs scalars, *Phys. Lett. B* **136**, 187 (1984).  
 [6] K. Agashe, R. Contino, and A. Pomarol, The minimal composite Higgs model, *Nucl. Phys.* **B719**, 165 (2005).  
 [7] N. Arkani-Hamed, A. G. Cohen, E. Katz, A. E. Nelson, T. Gregoire, and J. G. Wacker, The minimal moose for a little Higgs, *J. High Energy Phys.* **08** (2002) 021.

- [8] Z. Chacko, H.-S. Goh, and R. Harnik, Natural Electroweak Breaking from Mirror Symmetry, *Phys. Rev. Lett.* **96**, 231802 (2006).
- [9] N. Arkani-Hamed, A. G. Cohen, E. Katz, and A. E. Nelson, The littlest Higgs, *J. High Energy Phys.* **07** (2002) 034.
- [10] J. A. Aguilar-Saavedra, Identifying top partners at LHC, *J. High Energy Phys.* **11** (2009) 030.
- [11] J. Berger, J. Hubisz, and M. Perelstein, A fermionic top partner: Naturalness and the LHC, *J. High Energy Phys.* **07** (2012) 016.
- [12] M. Buchkremer, G. Cacciapaglia, A. Deandrea, and L. Panizzi, Model independent framework for searches of top partners, *Nucl. Phys.* **B876**, 376 (2013).
- [13] J. H. Kim and I. M. Lewis, Loop induced single top partner production and decay at the LHC, *J. High Energy Phys.* **05** (2018) 095.
- [14] H. Alhazmi, J. H. Kim, K. Kong, and I. M. Lewis, Shedding light on top partner at the LHC, *J. High Energy Phys.* **01** (2019) 139.
- [15] A. Anandakrishnan, J. H. Collins, M. Farina, E. Kuflik, and M. Perelstein, Odd top partners at the LHC, *Phys. Rev. D* **93**, 075009 (2016).
- [16] M. J. Dolan, J. L. Hewett, M. Krämer, and T. G. Rizzo, Simplified models for Higgs physics: Singlet scalar and vectorlike quark phenomenology, *J. High Energy Phys.* **07** (2016) 039.
- [17] M. Chala, R. Gröber, and M. Spannowsky, Searches for vector-like quarks at future colliders and implications for composite Higgs models with dark matter, *J. High Energy Phys.* **03** (2018) 040.
- [18] S. Gopalakrishna, T. Mandal, S. Mitra, and G. Moreau, LHC signatures of warped-space vectorlike quarks, *J. High Energy Phys.* **08** (2014) 079.
- [19] R. Dermisek, E. Lunghi, and S. Shin, Hunting for vectorlike quarks, *J. High Energy Phys.* **04** (2019) 019.
- [20] H. Han, L. Huang, T. Ma, J. Shu, T. M. P. Tait, and Y. Wu, Six top messages of new physics at the LHC, *J. High Energy Phys.* **10** (2019) 008.
- [21] S. Colucci, B. Fuks, F. Giacchino, L. Lopez Honorez, M. H. G. Tytgat, and J. Vandecasteele, Top-philic vectorlike portal to scalar dark matter, *Phys. Rev. D* **98**, 035002 (2018).
- [22] B. A. Dobrescu and F. Yu, Exotic signals of vector-like quarks, *J. Phys. G* **45**, 08LT01 (2018).
- [23] S. Gopalakrishna, T. S. Mukherjee, and S. Sadhukhan, Extra neutral scalars with vectorlike fermions at the LHC, *Phys. Rev. D* **93**, 055004 (2016).
- [24] S. Dasgupta, R. Pramanick, and T. S. Ray, Broad toplike vector quarks at LHC and HL-LHC, *Phys. Rev. D* **105**, 035032 (2022).
- [25] G. Corcella, A. Costantini, M. Ghezzi, L. Panizzi, G. M. Pruna, and J. Šalko, Vector-like quarks decaying into singly and doubly charged bosons at LHC, *J. High Energy Phys.* **10** (2021) 108.
- [26] R. Dermisek, E. Lunghi, N. McGinnis, and S. Shin, Tau-jet signatures of vectorlike quark decays to heavy charged and neutral Higgs bosons, *J. High Energy Phys.* **08** (2021) 159.
- [27] K. du Plessis, M. M. Flores, D. Kar, S. Sinha, and H. van der Schyf, Hitting two BSM particles with one lepton-jet: Search for a top partner decaying to a dark photon, resulting in a lepton-jet, *SciPost Phys.* **13**, 018 (2022).
- [28] T. G. Rizzo, Kinetic mixing and portal matter phenomenology, *Phys. Rev. D* **99**, 115024 (2019).
- [29] T. G. Rizzo, Portal matter and dark sector phenomenology at colliders, in *Proceedings of the Snowmass Summer Study, 2022* (2022), 2, [arXiv:2202.02222](https://arxiv.org/abs/2202.02222).
- [30] X. Qin and J.-F. Shen, Search for single production of vector-like  $B$  quark decaying to a Higgs boson and bottom quark at the CLIC, *Nucl. Phys.* **B966**, 115388 (2021).
- [31] G. N. Wojcik, Kinetic mixing from Kaluza-Klein modes: A simple construction for portal matter, [arXiv:2205.11545](https://arxiv.org/abs/2205.11545).
- [32] M. Fabbrihesi, E. Gabrielli, and G. Lanfranchi, The dark photon, [arXiv:2005.01515](https://arxiv.org/abs/2005.01515).
- [33] R. Foot and S. Vagnozzi, Solving the small-scale structure puzzles with dissipative dark matter, *J. Cosmol. Astropart. Phys.* **07** (2016) 013.
- [34] J. H. Kim, S. D. Lane, H.-S. Lee, I. M. Lewis, and M. Sullivan, Searching for dark photons with Maverick top partners, *Phys. Rev. D* **101**, 035041 (2020).
- [35] M. Aaboud *et al.* (ATLAS Collaboration), Search for single production of vector-like quarks decaying into  $Wb$  in  $pp$  collisions at  $\sqrt{s} = 13$  TeV with the ATLAS detector, *J. High Energy Phys.* **05** (2019) 164.
- [36] M. Aaboud *et al.* (ATLAS Collaboration), Search for pair production of heavy vector-like quarks decaying into hadronic final states in  $pp$  collisions at  $\sqrt{s} = 13$  TeV with the ATLAS detector, *Phys. Rev. D* **98**, 092005 (2018).
- [37] A. M. Sirunyan *et al.* (CMS Collaboration), Cross section measurement of  $t$ -channel single top quark production in  $pp$  collisions at  $\sqrt{s} = 13$  TeV, *Phys. Lett. B* **772**, 752 (2017).
- [38] A. M. Sirunyan *et al.* (CMS Collaboration), Measurement of top quark pair production in association with a Z boson in proton-proton collisions at  $\sqrt{s} = 13$  TeV, *J. High Energy Phys.* **03** (2020) 056.
- [39] N. Bizot, G. Cacciapaglia, and T. Flacke, Common exotic decays of top partners, *J. High Energy Phys.* **06** (2018) 065.
- [40] K.-P. Xie, G. Cacciapaglia, and T. Flacke, Exotic decays of top partners with charge  $5/3$ : Bounds and opportunities, *J. High Energy Phys.* **10** (2019) 134.
- [41] G. Cacciapaglia, T. Flacke, M. Park, and M. Zhang, Exotic decays of top partners: Mind the search gap, *Phys. Lett. B* **798**, 135015 (2019).
- [42] M. Chala, Direct bounds on heavy toplike quarks with standard and exotic decays, *Phys. Rev. D* **96**, 015028 (2017).
- [43] J. A. Aguilar-Saavedra, D. E. López-Fogliani, and C. Muñoz, Novel signatures for vector-like quarks, *J. High Energy Phys.* **06** (2017) 095.
- [44] R. Benbrik *et al.*, Signatures of vector-like top partners decaying into new neutral scalar or pseudoscalar bosons, *J. High Energy Phys.* **05** (2020) 028.

- [45] A. Bhardwaj, T. Mandal, S. Mitra, and C. Neeraj, Roadmap to explore the vectorlike quarks decaying to a new (pseudo) scalar, *Phys. Rev. D* **106**, 095014 (2022).
- [46] K. Das, T. Mondal, and S. K. Rai, Nonstandard signatures of vectorlike quarks in a leptophobic 221 model, *Phys. Rev. D* **99**, 115002 (2019).
- [47] S. Banerjee, D. Barducci, G. Bélanger, and C. Delaunay, Implications of a high-mass diphoton resonance for heavy Quark searches, *J. High Energy Phys.* **11** (2016) 154.
- [48] A. Banerjee, D. B. Franzosi, and G. Ferretti, Modelling vector-like quarks in partial compositeness framework, *J. High Energy Phys.* **03** (2022) 200.
- [49] A. Banerjee *et al.*, Phenomenological aspects of composite Higgs scenarios: Exotic scalars and vector-like quarks, [arXiv:2203.07270](https://arxiv.org/abs/2203.07270).
- [50] M. Ciuchini, E. Franco, S. Mishima, and L. Silvestrini, Electroweak precision observables, new physics and the nature of a 126 GeV Higgs boson, *J. High Energy Phys.* **08** (2013) 106.
- [51] J. de Blas, M. Ciuchini, E. Franco, S. Mishima, M. Pierini, L. Reina, and L. Silvestrini, Electroweak precision observables and Higgs-boson signal strengths in the Standard Model and beyond: Present and future, *J. High Energy Phys.* **12** (2016) 135.
- [52] C.-Y. Chen, S. Dawson, and E. Furlan, Vectorlike fermions and Higgs effective field theory revisited, *Phys. Rev. D* **96**, 015006 (2017).
- [53] A. M. Sirunyan *et al.* (CMS Collaboration), Search for top squark production in fully-hadronic final states in proton-proton collisions at  $\sqrt{s} = 13$  TeV, *Phys. Rev. D* **104**, 052001 (2021).
- [54] M. Aaboud *et al.* (ATLAS Collaboration), Search for invisible particles produced in association with single top quarks in proton-proton collisions at  $\sqrt{s} = 13$  TeV with the ATLAS detector, Report No. ATLAS-CONF-2022-036.
- [55] S. Kraml, U. Laa, L. Panizzi, and H. Prager, Scalar versus fermionic top partner interpretations of  $t\bar{t} + E_T^{\text{miss}}$  searches at the LHC, *J. High Energy Phys.* **11** (2016) 107.
- [56] T. Robens and T. Stefaniak, Status of the Higgs singlet extension of the standard model after LHC Run 1, *Eur. Phys. J. C* **75**, 104 (2015).
- [57] T. Robens, Investigating extended scalar sectors at current and future colliders, *Proc. Sci. LHCP2019* (2019) 138.
- [58] T. Robens, More doublets and singlets, in *Proceedings of the 56th Rencontres de Moriond on Electroweak Interactions and Unified Theories* (2022), 5, [arXiv:2205.06295](https://arxiv.org/abs/2205.06295).
- [59] S. Adhikari, S. D. Lane, I. M. Lewis, and M. Sullivan, Complex scalar singlet model benchmarks for snowmass, in *Proceedings of Snowmass 2021* (2022), 3, [arXiv:2203.07455](https://arxiv.org/abs/2203.07455).
- [60] T. Robens, Constraining extended scalar sectors at current and future colliders: An update, in *Proceedings of the 8th Workshop on Theory, Phenomenology and Experiments in Flavour Physics: Neutrinos, Flavor Physics and Beyond*, 9, 2022, [arXiv:2209.15544](https://arxiv.org/abs/2209.15544).
- [61] CMS Collaboration, Search for Higgs boson decays to invisible particles produced in association with a top-quark pair or a vector boson in proton-proton collisions at  $\sqrt{s} = 13$  TeV and combination across Higgs production modes, CERN Report No. CMS-PAS-HIG-21-007.
- [62] ATLAS Collaboration, Combination of searches for invisible decays of the Higgs boson using  $139 \text{ fb}^{-1}$  of proton-proton collision data at  $\sqrt{s} = 13$  TeV collected with the ATLAS experiment, CERN Report No. CERN-EP-2022-289.
- [63] P. A. Zyla *et al.* (Particle Data Group), Review of particle physics, *Prog. Theor. Exp. Phys.* **2020**, 083C01 (2020).
- [64] J. Jaeckel and A. Ringwald, The low-energy frontier of particle physics, *Annu. Rev. Nucl. Part. Sci.* **60**, 405 (2010).
- [65] S. Davidson, B. Campbell, and D. Bailey, Limits on particles of small electric charge, *Phys. Rev. D* **43**, 2314 (1991).
- [66] J. W. Brockway, E. D. Carlson, and G. G. Raffelt, SN1987A gamma-ray limits on the conversion of pseudoscalars, *Phys. Lett. B* **383**, 439 (1996).
- [67] J. Alwall, R. Frederix, S. Frixione, V. Hirschi, F. Maltoni, O. Mattelaer, H.-S. Shao, T. Stelzer, P. Torrielli, and M. Zaro, The automated computation of tree-level and next-to-leading order differential cross sections, and their matching to parton shower simulations, *J. High Energy Phys.* **07** (2014) 079.
- [68] A. Alloul, N. D. Christensen, C. Degrande, C. Duhr, and B. Fuks, FeynRules 2.0: A complete toolbox for tree-level phenomenology, *Comput. Phys. Commun.* **185**, 2250 (2014).
- [69] C. Degrande, C. Duhr, B. Fuks, D. Grellscheid, O. Mattelaer, and T. Reiter, UFO: The universal FeynRules output, *Comput. Phys. Commun.* **183**, 1201 (2012).
- [70] R. D. Ball *et al.*, Parton distributions with LHC data, *Nucl. Phys.* **B867**, 244 (2013).
- [71] C. Bierlich *et al.*, A comprehensive guide to the physics and usage of PYTHIA 8.3, [arXiv:2203.11601](https://arxiv.org/abs/2203.11601).
- [72] T. Sjostrand, S. Mrenna, and P. Z. Skands, PYTHIA 6.4 physics and manual, *J. High Energy Phys.* **05** (2006) 026.
- [73] T. H. Park, Jet energy resolution measurement of the ATLAS detector using momentum balance, <https://cds.cern.ch/record/2642494>.
- [74] V. Khachatryan *et al.* (CMS Collaboration), Jet energy scale and resolution in the CMS experiment in pp collisions at 8 TeV, *J. Instrum.* **12**, P02014 (2017).
- [75] J. de Favereau, C. Delaere, P. Demin, A. Giammanco, V. Lemaître, A. Mertens, and M. Selvaggi (DELPHES 3 Collaboration), DELPHES 3: A modular framework for fast simulation of a generic collider experiment, *J. High Energy Phys.* **02** (2014) 057.
- [76] D. E. Kaplan, K. Rehermann, M. D. Schwartz, and B. Tweedie, Top Tagging: A Method for Identifying Boosted Hadronically Decaying Top Quarks, *Phys. Rev. Lett.* **101**, 142001 (2008).
- [77] M. Cacciari, G. P. Salam, and G. Soyez, FastJet user manual, *Eur. Phys. J. C* **72**, 1896 (2012).
- [78] S. Bentvelsen and I. Meyer, The Cambridge jet algorithm: Features and applications, *Eur. Phys. J. C* **4**, 623 (1998).
- [79] O. Matsedonskyi, G. Panico, and A. Wulzer, On the interpretation of top partners searches, *J. High Energy Phys.* **12** (2014) 097.
- [80] N. Kidonakis, Higher-order corrections for  $t\bar{t}$  production at high energies, in *Proceedings of the 2022 Snowmass Summer Study* (2022), 3, [arXiv:2203.03698](https://arxiv.org/abs/2203.03698).
- [81] A. Kulesza, L. Motyka, D. Schwartländer, T. Stebel, and V. Theeuwes, Associated production of a top quark pair with a heavy electroweak gauge boson at NLO + NNLL accuracy, *Eur. Phys. J. C* **79**, 249 (2019).

- [82] N. Kidonakis and N. Yamanaka, Higher-order corrections for  $tW$  production at high-energy hadron colliders, *J. High Energy Phys.* **05** (2021) 278.
- [83] M.L. Mangano, M. Moretti, and R. Pittau, Multijet matrix elements and shower evolution in hadronic collisions:  $Wb\bar{b} + n$  jets as a case study, *Nucl. Phys.* **B632**, 343 (2002).
- [84] C. Lester and D. Summers, Measuring masses of semi-invisibly decaying particle pairs produced at hadron colliders, *Phys. Lett. B* **463**, 99 (1999).
- [85] F. Maltoni, G. Ridolfi, and M. Ubiali, b-initiated processes at the LHC: A reappraisal, *J. High Energy Phys.* **07** (2012) 022.